709

Final report on implementation and quality of the D-FIRE assimilation system

J. W. Kaiser[1,2,3], A. Heil[4],
M. G. Schultz[4], S.Remy[2], O. Stein[4],
G. R. van der Werf[5], M. J. Wooster[1],
and W. Xu[1,6]

Research Department

July 2013

KCL, London, UK
ECMWF, Reading, UK
MPIC, Mainz, DE
FZJ, Jülich, DE
VU, Amsterdam, NL
PML, Plymouth, UK

This report has been submitted to EU in December 2011
as deliverable D_D-FIRE_7 of the MACC project.
Several references and URLs have been updated in this Tech Memo

Series: ECMWF Technical Memoranda

A full list of ECMWF Publications can be found on our web site under:
http://www.ecmwf.int/publications/

Contact: library@ecmwf.int

Table of contents

1 Introduction

D-FIRE is responsible for the provision of accurate emission estimates from open biomass burning for use in the global and regional MACC data assimilation and modelling systems. These estimates are required in near real time (NRT) as well as retrospectively for reanalysis purposes. Even though the primary intended use is project internal all D-FIRE products are publicly available. D-FIRE builds on the global fire assimilation system GFASv0 implemented by GEMS, which uses satellite-based fire radiative power (FRP) observations, and on the retrospective global fire emission database GFEDv2.

The GFED system has been upgraded from version 2 to version 3, which is based on burnt area observations instead of hot spot observations. Its retrospective monthly fire emissions have been produced for 1997-2010. Additionally, a combination of GFAS and GFED has been used to provide daily fire emissions during 2003-2008, which have been used in the MACC reanalysis.

The GFAS has been developed further. One of the major new features is the use of land cover-specific conversion factors for relating FRP to dry matter combustion rate. These factors are chosen such that the FRP-based GFASv1.0 products are consistent with the burnt area-based GFEDv3.1. Therefore, GFASv1.0 combines the information of GFEDv3.1 and the FRP observations in real time. Following user requests the list of species has been extended to 40 smoke components. GFAS has been used to reprocess the FRP observations since 2003 and to produce daily global fire emission estimates in real time throughout the project.

The validation in D-FIRE has included comparisons between the independent FRP and burnt area observation-derived products in GFAS and GFEDv3. Further validation of the D-FIRE products, based on atmospheric observations, has been performed in extensive collaborations with the global aerosol and reactive gas sub-projects of MACC.

On overview of D-FIRE with links to its products can be found at http://gmes-atmosphere.eu/fire/.

In this report, Sect. 2 gives an overview of the D-FIRE products. Sect. 2.1 describes how D-FIRE generates suitable FRP products from the observations by the MODIS, SEVIRI and GOES satellite instruments. The assimilation of these products in the different versions of GFAS is described in Sect. 2.2 and the calculation of emission fluxes in GFAS and GFED is described in Sect. 2.3. Sect. 3 gives an overview of the use of the D-FIRE products in MACC and beyond. It also contains conclusions on the accuracy of the products that have been reached during the use of the D-FIRE products. Finally, Sect. 4 summarises the findings and Sect. 5 lists publications and presentations by D-FIRE, in which further information can be found.

2 Product Overview

An overview of the data services delivered by D-FIRE is given in Table 1. The "archive ID" refers to the experiment ID with which the data are stored in the MARS archive at ECMWF. More information on MARS retrievals and the GRIB data format is available at http://gmes-atmosphere.eu/about/project_structure/input_data/d_fire/ProductsInMARS/. All GFASv1.0 data is also available in NetCDF format at http://join.iek.fz-juelich.de/macc/access?catalog=http://ows-server.iek.fz-juelich.de/MACC_gfas10_daily_sfc. The GFEDv3.1 data is also available in ASCII format at http://www.globalfiredata.org/. GFASv1.0 and GFEDv3.1 are also available in ASCII and NetCDF at http://eccad.sedoo.fr. The products are described in more detail in the following subsections.

Table 1: Overview of D-FIRE products.

Description	Temp. resol. (hrs)	Spat. resol. (deg)	Temp. Coverage	Archive id	Input	Label
gridded satellite FRP products						
GOES East	1	0.5	7/2010 – NRT	ffsx	UCAR	
GOES West	1	0.5	7/2010 – NRT	ffsw	UCAR	
SEVIRI	1	0.5	9/2007 – NRT	fft5	LandSAF	
MODIS Terra	1	0.5	1/2003–9/12/2012	fbl5	NOAA, NASA (MOD14)	
MODIS Aqua	1	0.5	1/2003–9/12/2012	fbl7	NOAA, NASA (MOD14)	
MODIS Terra	1	0.5	1/12/2012 – NRT	fslr	NOAA, NASA (MOD14)	
MODIS Aqua	1	0.5	1/12/2012 – NRT	fsls	NOAA,NASA (MOD14)	
MODIS Terra	1	0.1	1/12/2012 – NRT	fspr	NOAA, NASA (MOD14)	
MODIS Aqua	1	0.1	1/12/2012 – NRT	fsps	NOAA, NASA (MOD14)	
MODIS Aqua and Terra, SEVIRI, GOES East and West	1/24	0.1 and 0.5	1/2005 – NRT	fx5h	NOAA, NASA (MOD14), LandSAF, KCL (GOES)	GFASv1.1
Merged / assimilated FRP products						
merged MODIS and SEVIRI	24	~1.1	10/2008 – NRT	n/a (ECFS)	NOAA, NASA (MOD14), LandSAF	GFASv0
assimilated MODIS	24	0.1	1/2003 – 12/2010	f922	NOAA, NASA (MOD14)	
assimilated MODIS	24	0.5	1/2003 – NRT	ffxr	fbl5, fbl7	GFASv1.0
assimilated MODIS	24	0.1	3/2011 – NRT	fl6z	fhtr, fhts	GFASv1.1
assimilated MODIS	24	0.1 and 0.5	1/2005 – NRT	fx5h	NOAA, NASA (MOD14)	GFASv1.1
Emission products						
GFEDv3.0	1 month	0.5	1/1997 – 12/2008	fa5z	VUA	GFEDv3.0
GFEDv3.1	1 month	0.5	1/1997 – 12/2009	fhhi	VUA	GFEDv3.1
reanalysis	24	0.1	1/2003 – 12/2008	fagg	fa5z, f922	
GFASv0	24	~1.1	10/2008 – NRT	f7i1, f7i2	NOAA, NASA, LandSAF	GFASv0
GFASv1.0	24	0.5	1/2003 – NRT	ffxr	fbl5, fbl7 until 1/12/2012, then fslr and fsls	GFASv1.0
GFASv1.1	24	0.1	3/2011 – NRT	fl6z	fl6x, fl6y until 1/12/2012, then fspr and fsps	GFASv1.1
GFASv1.1	24	0.1 and 0.5	1/2005 – NRT	fx5h	NOAA, NASA, LandSaf and KCL	GFASv1.1

2.1 Gridded Satellite FRP Products

Earth Observation satellite sensors play an important role within MACC in quantifying biomass burning related fuel consumption dynamics through measurements of fire radiative power (which is used as a surrogate measure for fuel consumption rate; Wooster *et al.,* 2005). This type of EO data allows the D-FIRE system to capture the spatial and temporal variability of fire emissions, which are globally significant for many aerosol and trace gas species and very much larger in terms of their variability than are industrial emissions. Polar-orbiting sensors like MODIS offer global coverage and finer spatial resolution, and thus improved detection performance for smaller (low FRP) fires (Freeborn *et al.,* 2011). However the prolonged periods between overpasses (which can be many hours) hinders reconstruction of the fire diurnal cycle, and also provides only a few opportunities a day to image the fires of each area (which can be problematic in particularly cloudy regions). Polar orbiting sensors also deliver data having time-varying geometric characteristics, which can induce variability into the measured signals. By contrast, geostationary sensors offer the advantages of a much higher temporal resolution, and a constant viewing geometry at any particular point on the Earth. However, due to the coarser spatial resolution of the observations, they miss smaller (lower FRP) fires, and at the regional scale this results in for example Meteosat SEVIRI typically then underestimating total summed FRP when compared to MODIS (e.g. when the observed FRP is integrated over one day and, say, a 100 km x 100 km area). Therefore, ultimately it is necessary to exploit both types of satellite FRP data if D-FIRE is to feed the best biomass burning emissions record into the MACC system.

All satellite FRP products are acquired and archived at ECMWF by the MACC sub-project D-SAT. They are subsequently gridded and further processed.

2.1.1 MODIS

The MODIS fire products MOD14 and geolocation products MOD03 from the instruments aboard the polar orbiting satellites Terra and Aqua are acquired by ftp pull from NOAA up to March 2011 and from NASA since. They have a native resolution of 1 km. The gridding of these products onto a global grid is described in detail in Kaiser et al. BG 2012. The geolocation of detected fires is contained in MOD14 but the one for detections of no fire burning is only available in MOD14, which are two orders of magnitude larger. MOD14 dating back to 2003 has also been downloaded from NASA. The download of MOD03 is still going on.

An approximation form the pixel location in each MODIS granule has been developed in order to be able to process no-fire observations in GFAS even without MOD03. The approximation has an accuracy of about 10 km. Since the geolocation of detected fires is read from MOD14, the limited accuracy of the approximation affects only the correction for partial cloud cover in GFAS. The approximation is used in GFASv1.0, which has a spatial resolution of about 50 km, but not in GFASv1.1, which has a resolution of about 10 km.

2.1.2 SEVIRI

The FRP_PIXEL and FRP_LIST fire products generated by the EUMETSAT Land SAF based within the *Instituto de Meteorologia* in Portugal is acquired via EUMETCAST. The products are derived from SEVIRI observations made onboard the geostationary satellite Meteosat-9. They have a high temporal frequency of four per hour and a spatial resolution of 3 km at the subsatellite point. The geolocation of all satellite pixels is available from static auxiliary datasets. The gridding procedure is

documented in Kaiser et al. ECMWF TM596 (2009). It is equivalent to the one used for MODIS described above.

The SEVIRI fire products have a bias w.r.t. MODIS because the active fire detection threshold of SEVIRI is larger (about 50MW vs. 10MW), and there are typically many more low FRP fires than high FRP fires. This bias is corrected in GFASv0 by simply doubling the SEVIRI fire observations, since Freeborn *et al.* (2009) and related works have shown the mean bias to be of this magnitude. Furthermore, the performance of GFAFv0 has shown that the SEVIRI observations far from the 'Earth disk' centre, specifically over South America and over central and northern Europe are rather unreliable, which is attributed to the very large viewing angles at these locations. This contributed to a severe underestimation of the Russian fires of 2010 in GFASv0, which were located just at the edge of the SEVIRI disk. As a consequence, the SEVIRI product over South America has been blacklisted in spring 2010. No action was taken concerning Europe, because GFASv0 is now superseded by GFASv1.0.

To counter this 'low spatial resolution bias' Freeborn et al. (2009) developed a 'virtual' FRP product with a 15 minute temporal resolution and a minimised FRP bias by combining polar orbiting and geostationary data. This product was able to deliver a fire radiative energy (FRE) estimate that contained the advantages of the geostationary characterisation of the fire diurnal cycle, but without the low spatial resolution bias. A different approach was used by Vermote et al. (2009) and Ellicott et al. (2009), whereby MODIS FRP observations were modulated by an assumed diurnal cycle in order to estimate the FRE emitted over a 0.5° area over an 8-day interval. Freeborn et al. (2011) built on this latter approach, enhancing the method to provide improved agreement between the FRE measures provided by MODIS and by SEVIRI over the same 8-day interval.

An approach to utilising this type of merging of polar orbiting and geostationary data types has now been explored for use with the FRP areal density data from the D-FIRE system. It is based on one year's assimilated FRP areal density data [2010] derived from the D-FIRE GFASv1.0 system, calculated separately from the MODIS and Meteosat SEVIRI sensors on an 8-daily basis at 0.5° and covering Africa, Europe and a small part of South America included in the SEVIRI imaging disk. Figure 1 demonstrates that at this spatio-temporal scale and for a location in North Africa, the SEVIRI FRP density data has a strong linear relationship with that from MODIS. In fact in all 0.5° cells in Africa where the fire activity is strong (i.e. outside of deserts, sparsely vegetated areas, humid tropical forests and grid cells containing large proportion of water), the relationship between MODIS and SEVIRI is similarly strong with a coefficient of determination (r^2) close to 1.

Since a clear linear relationship was found to exist for the type of 8-daily integrated FRP areal density data shown in Figure 1 for all significantly 'fire affected' grid cells, the existence of a similar relationship based on daily data was explored (since GFAS is designed to work at daily or better temporal resolutions). Figure 2 shows the results for the same grid cell as shown in Figure 1. The correlation is weaker than for the 8-daily FRP areal density data shown in Figure 1, and the slope reduced from 0.23 to 0.08. In this case, the differences may due to a few high FRP points seen by MODIS but not (apparently) by SEVIRI. Therefore, a thorough analysis of all the 0.5° grid cells in Africa was conducted to determine the degree of difference between the relationships found at 1 day and 8 day integration periods.
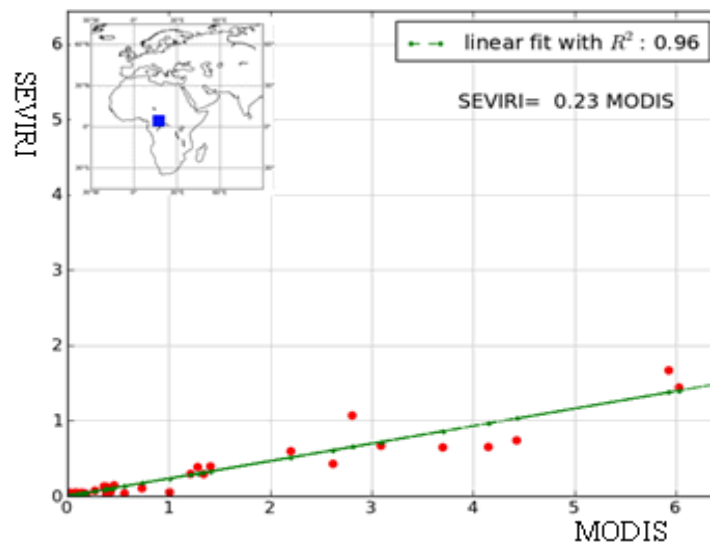
Figure 1: The relationship between MODIS and SEVIRI FRP areal density based on D-FIRE 8-daily FRP density totals for 2010, calculated for a 0.5° grid cell. The green line shows the least squares linear best fit between the two datasets. The blue square in the upper left corner shows the location of the grid cell in North Africa. Data are analysed at 5° spatial resolution.
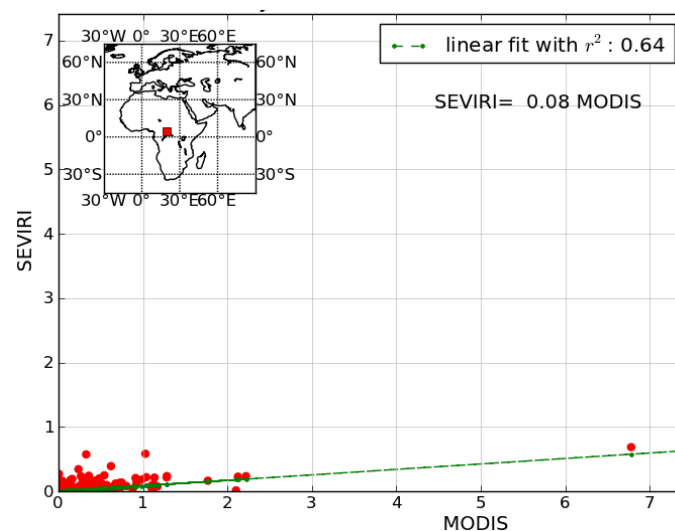

Figure 2: The relationship between MODIS and SEVIRI FRP areal density based on daily average in 2010, the red dots representing one days average FRP and the green line is a linear fitting between the two, the blue square in the upper left corner show the location of the grid cell in North Africa. Data are analysed at 5° spatial resolution.

Figure 3 shows the difference in slope between the linear best fits to the daily and 8-daily datasets. The majority of the slopes derived using the daily data are lower (blue to green colours) than for the same grid cell analysed with the 8 daily data. The mean difference equates to a 35% lower slope compared to 8 daily slope. The correlations are also generally lower for the daily than the 8 daily data (not shown).
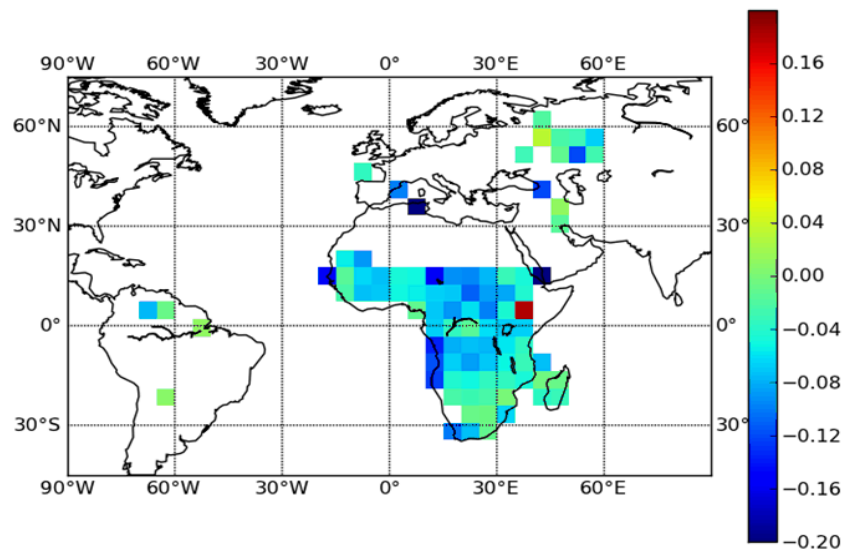
Figure 3: Difference in the slope of the linear best fit between the 8-daily and daily FRP density data from MODIS and SEVIRI, analysed as shown in Figure 1 and Figure 2 respectively. Blue to green colours indicate that the slope derived using daily FRP density data is lower than that using 8-daily FRP density data. Only grid cells showing significant fire activity in 2010 are analysed. Data are analysed at 5° spatial resolution.

Two key facts explain why the slope between the two FRP aerial density records is lower when you move to a daily temporal resolution. Firstly, as Figure 2 shows, for some grid cells there exists some occasional high FRP density records seen by MODIS that are not well viewed by SEVIRI. When integrating over 8-days, this type of 'outlier' is to some extent averaged out. Second, MODIS' view angle changes with an 8-daily revisit period (Freeborn *et al.,* 2011), so when integrating over just one day the view angle of the MODIS FRP aerial density record changes between records (whereas in the 8-day record this is essentially also averaged out). Since view angle has a large impact on the MODIS FRP observations (Freeborn *et al.,* 2011), even though the GFAS system reduces the weight weight of these high view angle observations (Kaiser *et al., BGD* 2011) they can have a significant impact on the relationship between the MODIS and SEVIRI FRP areal density observations made on a daily time step.

A second investigation focused on the improvement of the spatial resolution of the SEVIRI and MODIS FRP merging, since the resolution of GFAS is 0.5° but the examples considered initially (i.e. as shown in Figure 1 and Figure 2) were at 5°. Figure 4 shows the slopes derived at 0.5° based on the 8 days integration period, and although a strong linear relationship between SEVIRI and MODIS can be found, the proportion of grid cells where a usable relationship is found is far lower than at the 5° resolution (compare the number of grid cells in Figure 4 to Figure 3 for example). In a 0.5° grid cell there are only around 250 SEVIRI pixels at nadir (and far fewer near the disk edge), so it is quite likely that in a cell there is a relatively small number of SEVIRI (and matching MODIS) fire detections in any particular year - resulting in usable linear relationships only being found at a relatively small number of grid cells across the imaging disk. When using 5 ° grid cells, there exists two orders of magnitude more SEVIRI pixels in the cell - making the chance of having significant numbers of FRP observations within the cell very much higher and allowing a far greater proportion of the cells to return a usable slope value linking the SEVIRI and MODIS FRP density observations.
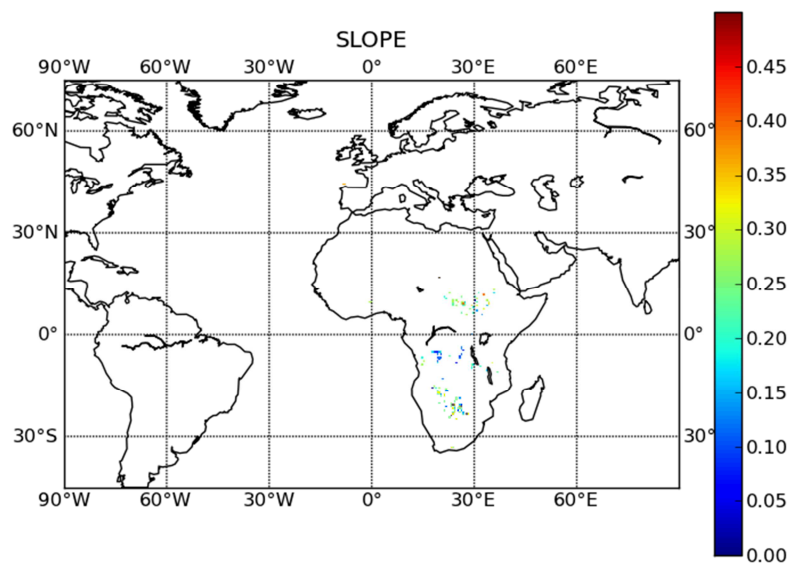
Figure 4: Slope of the linear best fit relationship between the 8-daily and daily FRP density data from MODIS and SEVIRI, analysed as shown in Figure 1 and Figure 2, respectively. Blue to green colours indicate that the slope derived using daily FRP density data is lower than that using 8-daily FRP density data. Only grid cells showing large fire activity in 2010 are analysed.

For the reasons highlighted above, a moving window strategy was adopted to investigate further the relationship between the SEVIRI and MODIS FRP density datasets output from the GFAS system at 0.5° and daily resolution. In this strategy, for each 0.5° grid cell, the surrounding 10 × 10 window (5° × 5°) is used to calculate the total FRP density from SEVIRI and MODIS, and then the relationship found using this 5° area is applied to this 0.5° cell. Using this method, a 0.5 ° resolution map of the slopes can be produced, either based on daily or 8-daily FRP density totals. Since the slope calculated using the 8-daily FRP data is believed to be more accurate (since it better avoids the 'outlier' and view angle variations highlighted earlier), the slope calculated using the 8-daily temporal resolution data was used, but the linear correlation coefficient (r) was also calculated for the daily temporal resolution data - as a record of how strong the linear relationship was between SEVIRI and MODIS at this temporal resolution, since it is at this temporal resolution that any final relationship will be used.

Figure 5 shows the result of this calculation. The relationship between the SEVIRI and MODIS FRP density data has a low slope (< 0.15) across most of Europe, whereas it is typically larger than this across Africa. The areas close to (0° , 0°), (30° E, 5° N) and (15° E, 15° S) have particularly large slopes, and almost half of the area of southern Africa demonstrates large slopes. Across the parts of South America seen by SEVIRI, the variance of the slope is large - probably reflecting the influence of the high SEVIRI view angles found here. The spatial pattern seen in the relationship between the MODIS and SEVIRI FRP data in

Figure 5 is similar to that of Freeborn *et al.* (2009; 2011), but the magnitude of the slopes are typically close to one half of that found therein (mean slope ~ 0.25 compared to ~ 0.5 in these published works). This is explained by the fact that whilst these papers worked on coincident SEVIRI and MODIS observations, the GFAS result is based on eight days' total FRP areal density data. According to the fire diurnal cycle, the MODIS instrument on the Aqua satellite overpasses at a daytime local solar time where fire activity is close to the peak, and so the time-integrated MODIS FRP density may be dominated by this observation in many cases. This is in contrast to SEVIRI, where the 96 observations

per day make the total SEVIRI FRP density an equally weighted sum of all observations over the full diurnal cycle.
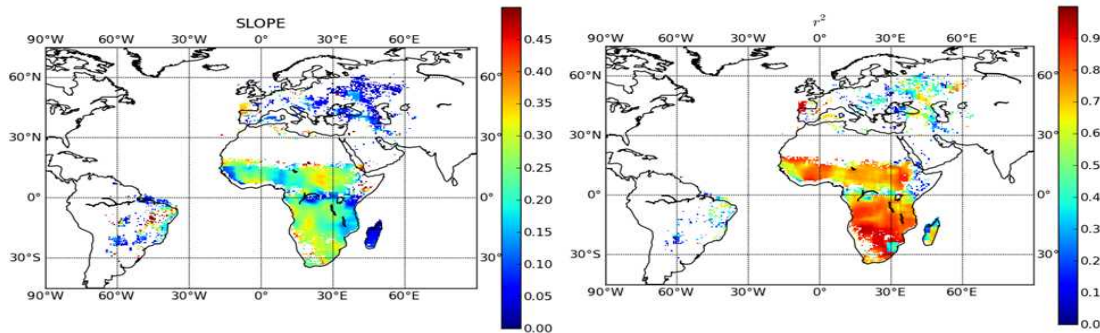

Figure 5: Relationships between the SEVIRI and MODIS FRP areal density data calculated using a 10 × 10 moving window of 0.5° grid cells, as described in the main text. (left) the slope calculated using the 8-daily FRP density data. (right) the coeffificent of variation (r²) based on the daily data.

The coefficient of variation shows a similar pattern to the slope. In Europe and South America the correlation is generally weak, but in Africa it is generally strong - reflecting the fact that there are many more fires in Africa and for most areas the viewing angle is lower than in Europe and South America.

Since the relationship between the SEVIRI and MODIS FRP areal density data in most of the significantly fire affected grid cells (which are located in Africa) is quite strong, it was considered feasible to try to use this relationship as the basis of the bias correction for the geostationary data. However, since over most of Europe and South America, the slope and coefficient of variation measures are low another solution was required for those areas. The relationship between the view angle and slope was therefore examined (

Figure 6).
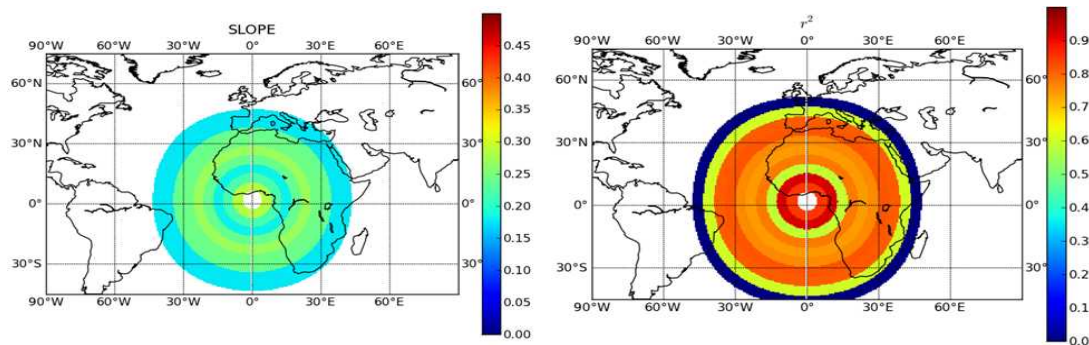
Figure 6: The slope and coefficient of variation between SEVIRI and MODIS FRP areal density measures as a function of the view angle of SEVIRI (5 ° steps). Data used were 8-daily FRP density data from GFAS.

The results in Figure 6 show that when the SEVIRI view angle is less than 5° (i.e. towards the sub-satellite point), there is no valid slope and the coefficient of variation is very low. This is a result of the fact that there is almost no land (and so no fires) within the 0 to 5 ° view angle range. From 10 - 20° the slope decreases view angle, from 20 to 30° the slope increases with view angle, and from 30 to 50°, it decreases once more. The same trend is found in the map of the coefficient of variation. In general therefore, the slope decreases with view angle reflecting the fact that SEVIRI misses more low

FRP fires as its pixel size increases, apart from the 10 - 20° range where a relative lack of fire activity in parts of the range cause the reverse.

The solution to the bias correction across the full SEVIRI disk was therefore to combine the information seen in Figure 5 and Figure 6. Figure 7 shows the final result of this, showing the slope calculated with the 8 daily data and the coefficient of variation with the daily data.
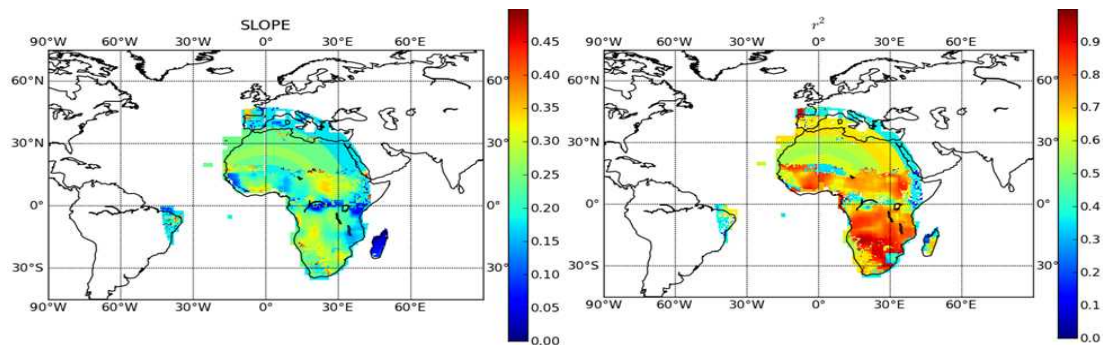

Figure 7: Final relationships between the SEVIRI and MODIS FRP areal density data of 2010, calculated using a 10 × 10 moving window of 0.5° grid cells (as described in the main text and shown in Figure 5), combined with the view angle dependent relationships seen in Figure 6 for view angles exceeding 50° or for areas having no data in Figure 5. (Left) The slope calculated using the 8-daily FRP density data. (Right) The coefficient of variation (r^2) based on the daily data. Via this combination, the whole of Africa and part of Europe and South America are filled by values, including even areas of the Sahara where there is no fire. If there are false alarms in the Sahara these should be masked out in any final product. Since there are many fires in Madagascar, although the view angle here exceeds 50° it makes sense to use the slope values from Figure 5 when the coefficient of variation for the grid cell exceeds 0.7.

The final result of applying the bias correction to the SEVIRI data of 2010 is shown in comparison to the MODIS data of the same year in Figure 8. The total FRP areal density data calculated from the bias adjusted SEVIRI data is 10,423 W m^{-2} for Africa, which is very close to the total MODIS FRP areal density of 9043 W m^{-2}.
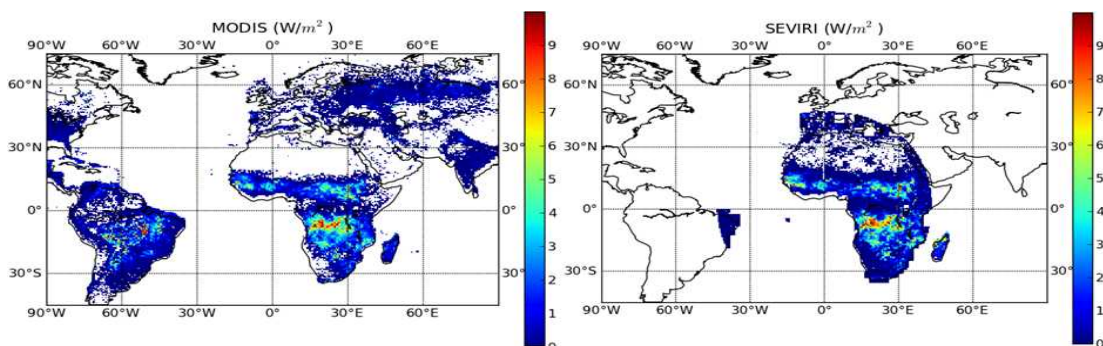

Figure 8: FRP areal density data of 2010. (left) the total FRP areal density deduced from MODIS. (right) the bias-adjusted FRP areal density data from SEVIRI, calculated by dividing the observed SEVIRI values by the slope (S) shown in Figure 7.

Figure 9 shows the histogram of the ratio of the two datasets (MODIS and bias-adjusted SEVIRI) shown in Figure 8, along with a direct comparison between the two. The strong degree of agreement proves that the slope data can be used to bias correct the SEVIRI FRP data to match the MODIS data - at least for the same year for which the slope is derived.
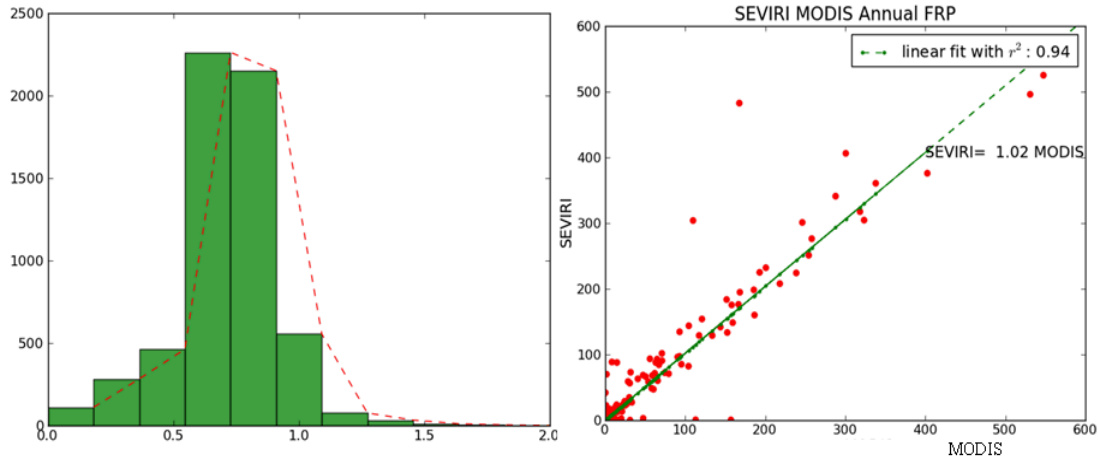

Figure 9: Comparison of daily bias-adjusted SEVIRI and daily MODIS FRP areal density data. (Left) Histogram of the ratios between these two datasets for 0.5 ° grid cells. The slope has a mean of 0.77 and a near Gaussian distribution. (Right) Scatterplot of the relationship between them, indicating a strong linear correlation with relatively few outliers.

In GFAS, the FRP areal data from Terra and Aqua is merged using:

$$\mathrm{FRP_m} = \left(\mathrm{FRP_T} \times \mathrm{CLM_T} + \mathrm{FRP_A} \times \mathrm{CLM_A} \right) \ / \ \left(\mathrm{CLM_T} + \mathrm{CLM_A} \right) \tag{1}$$

Where $\mathrm{FRP_m}$ is the daily merged MODIS FRP areal density calculated from both Terra and Aqua, $\mathrm{FRP_T}$ is the FRP density from Terra only, $1/\mathrm{CLM_T}$ is cloud cover density from Terra only, and $\mathrm{FRP_A}$ and $1/\mathrm{CLM_A}$ are, respectively, the same FRP density and cloud density data from Aqua.

A similar form of weighted averaging was derived to merge the SEVIRI and MODIS FRP areal density data, using the slope (S) and coefficient of variation (r²) shown in Figure 7.

$$\mathrm{FRP_{Tot}} = \left[\ \mathrm{FRP_m} \times \mathrm{CLM_m} + \left(1/S \right) \times \mathrm{FRP_S} \times \mathrm{R^2} \times \mathrm{CLM_S} \right] \ / \ \left(\mathrm{CLM_m} + \mathrm{R^2} \times \mathrm{CLM_S} \right) \tag{2}$$

where $\mathrm{FRP_{Tot}}$ is the merged FRP areal density from MODIS and SEVIRI together, $\mathrm{FRP_m}$ is the FRP density data from MODIS output from Equation (1), $1/\mathrm{CLM_m}$ is corresponding cloud areal density from MODIS, and $\mathrm{FRP_S}$ and $1/\mathrm{CLM_S}$ are the corresponding FRP areal density and cloud areal density data from SEVIRI. S and r² are, respectively, the slope between the eight daily FRP density data of SEVIRI and MODIS (shown in Figure 7 left) and the coefficient of variation calculated using the daily data (Figure 7 right). In cases where in a grid cell the FRP density from either MODIS or SEVIRI is zero, then the inverse of the cloud density for that sensor is also set to zero for this calculation, ensuring that the merged FRP density metric is calculated from the FRP density value that does have a value.

However, before Equation (2) could be used with assurance the system required validation to determine whether it could be confidently applied to years other than those included in the slope derivation. Data from 2009 was used for this purpose, with the bias adjustment based on the 2010 slope derivations already shown. Figure 10 shows the results of this application, where the spatial

pattern looks similar to that shown in Figure 8 for 2010 but with the bias-adjusted SEVIRI FRP areal density somewhat larger than that of MODIS (13000 W m^{-2} *vs.* 8090 W m^{-2}). The histogram of Figure 10 shows once again a normal Gaussian distribution, but with a higher mean of 0.9 and with nearly a third of the grid cells having slopes exceeding 1.0 (most located in South America). The linear regression between the bias adjusted SEVIRI and MODIS FRP areal density data also has a slope much greater than 1.0 (1.55). These differences may be explained by that the fire activity in 2010 was larger than in 2009, with a total of MODIS FRP areal density of 9341 W m^{-2} in 2010 and 8090 W m^{-2} in 2009, and that the relationship between SEVIRI and MODIS (which depends on the degree to which the former sensor fails to detect low FRP fires) is itself dependent on the fire activity.
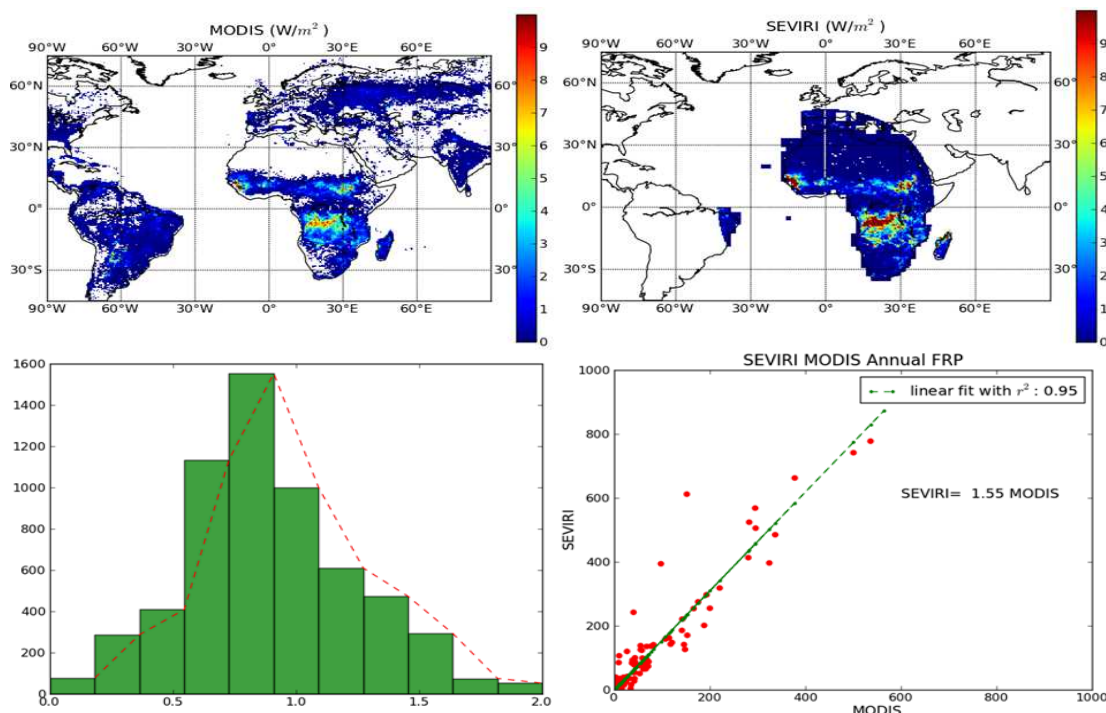

Figure 10: Results obtained when applying the slopes derived using the 2010 data to the data of 2009 (see Figure 8 and Figure 9 for details of the individual frames of this Figure). The histogram of slope between MODIS and corrected SEVIRI data in 2009 and the relationship between them.

For this reason, application of Equation (2) should be considered carefully. It is very likely not sufficient to derive the slope information from a single year and apply it to future years, but rather a moving monthly or seasonal window would need to be used to continually update the slope values. Via this procedure, an FRP areal density metric making full use of both polar orbiting and geostationary datasets can be produced for deriving the fuel consumption measures that drive the trace gas and aerosol emissions within the GFAS system, increasing the number of observations used at each grid cell location by more than an order of magnitude. Further data will be needed to test this, but since GFAS is moving to a sub-daily time step in future we will prioritize instead the investigation and implementation of an alternative method of bias correcting the SEVIRI data, based on the actual ratio of the SEVIRI to MODIS FRP density data calculated when co-incident observations are available (typically ~ 4 to 8 times per day), and then interpolated to an hourly time step and applied to the hourly GFAS SEVIRI FRP areal density products.

2.1.3 GOES East and West

A system for the near real time detection of active fires and characterisation of their fire radiative power (FRP) for MACC has been developed for use with data from the Geostationary Operational Environmental Satellites (GOES) viewing South, North and Central America. The purpose is to extend the coverage of the geostationary data used within MACC beyond that provided by SEVIRI. The system runs in real-time and is fully automatic, based on GOES data received at KCL from the University Corporation for Atmospheric Research (UCAR, http://www2.ucar.edu/) and with results uploaded to ECMWF in real-time.

Real time GOES East and GOES West data at half hourly temporal resolution is downloaded from UCAR with McIDAS. McIDAS is a suite of applications for analysing and displaying meteorological data for research and education. The system has been running at KCL for nearly two years, and has been continually updated and improved in response to feedback from the D-FIRE team, particularly ECMWF. In 2011, the algorithms used in the processing chain were updated to deliver a per-pixel atmospheric transmittance correction to the FRP, together with an FRP uncertainty estimate. The former is based on multiple runs of a radiative transfer model, whose results were then used to derive an empirical bit-fit relationship between atmospheric water vapour concentration and middle infrared atmospheric transmittance as is already performed for SEVIRI in the context of the LSA SAF FRP_PIXEL product. ECMWF is providing the water vapour data of the operational weather forecast to KCL. The per-pixel FRP uncertainty estimate is also based on the methodology used to derive FRP uncertainties within the LSA SAF Meteosat SEVIRI operational FRP products, which are already assimilated into the MACC system in test mode. The methodology for the atmospheric transmittance correction and the per-pixel FRP uncertainty estimate are described in the FRP Pixel Product Guides available on the LSA SAF web site (http://landsaf.meteo.pt/). These improvements in the FRP metric and in the estimate of uncertainty make the GOES FRP products provided to MACC fully compatible with the existing SEVIRI FRP products, and ultimately should improve the estimates of dry matter fuel consumption and trace gas/aerosol emissions over the America's within the MACC system, since the temporal resolution provided by GOES is around an order of magnitude higher than the MODIS-only system.

The detail of the GOES data processing chain developed and operating at KCL is based on the same fire detection code and FRP algorithm developed for SEVIRI (Roberts and Wooster, 2008), but with some adaptations for use with GOES. These adaptations include a full cloud screening algorithm, since the UCAR GOES feed does not provide a cloud mask. The final GOES algorithm is fully described in Xu *et al.* (2010). Fire detections output from the GOES processing chain, such as those shown in Figure 11, were validated via a direct comparison to MODIS (Figure 12).

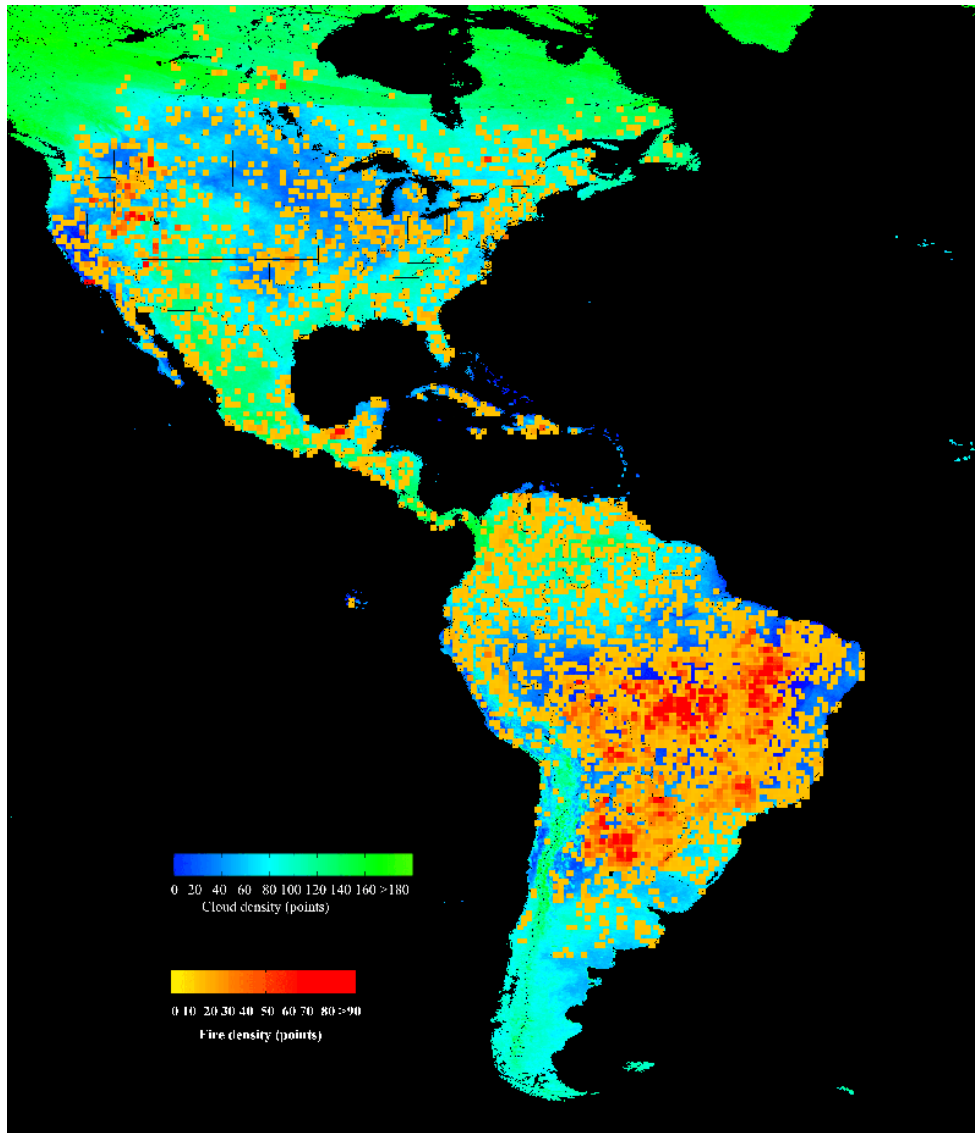*Figure 11: Total active fire and cloud detections made during July 2007 from GOES East. Cloud density is expressed as the total number of cloudy pixels detected during the month in 0.05 × 0.05 ° grid cells, whilst fire pixel density is expressed as the total number of active fire pixels detected in larger 0.5 × 0.5 ° grid cells over the same period (since fires are generally far less frequent than cloud).*
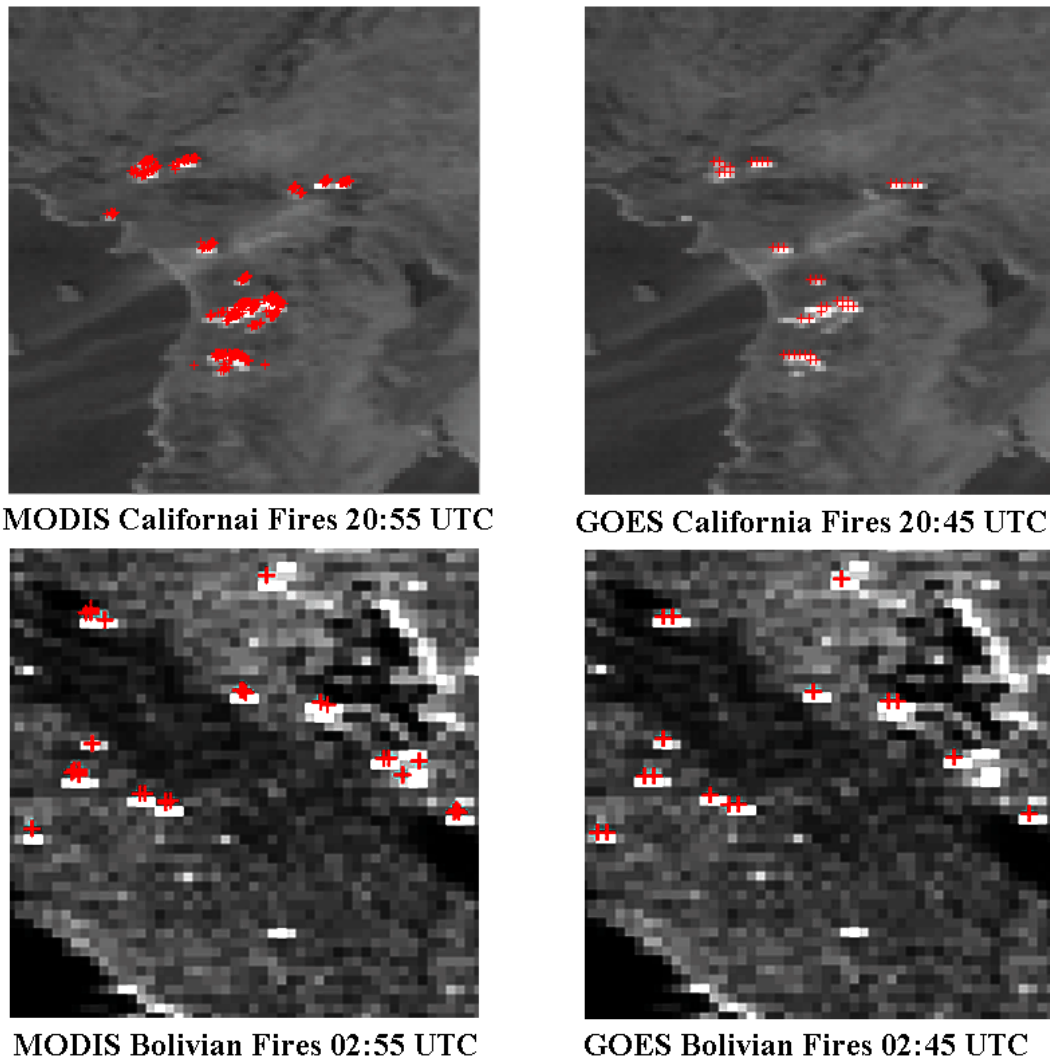
Figure 12: Comparison between the active fire detections made by MODIS (left) and GOES (right) over California (top; on 22 October 2007) and Brazil (bottom; on 11 August 2008). The background image is the GOES MIR – TIR brightness temperature difference image (BT_DIFF). Fires appear bright white in this rendition, and the active fire detections from each sensor are highlighted as red crosses. The spatial extent of each sub image is approximately 460 km x 800 km. In each case the MODIS image was taken within 10 minutes of the corresponding GOES scene, and one GOES fire detection can correspond to many MODIS fire pixel detections, due to the sensor spatial resolution differences.

The comparisons between MODIS and GOES active fire detections indicate that the GOES fire detection algorithm shows a relatively low incidence of false alarms comparable to that reported for SEVIRI (Roberts and Wooster, 2008; Schroeder *et al.,* 2008), and somewhat lower than the GOES ABBA apparent false alarm rate reported by Hoffman et al. (2007). Errors of omission for fire pixels having FRP > 30 MW are less than 10% (omission errors of ~ 50% are seen when considering fire pixels of all magnitudes, as is expected as GOES cannot detect low FRP fire pixels due to its coarse spatial resolution). These results are very similar to those seen from SEVIRI FRP Pixel product (Roberts and Wooster, 2008).

In terms of FRP measures, clusters of fire pixels having MIR brightness temperatures < 335 K (the stated GOES saturation value) show a relatively strong agreement between the GOES and MODIS-measured FRP (Figure 13). For fires including possibly saturated pixels (BT_{MIR} > 335 K) the relationship is less strong, and some FRP underestimation by GOES is apparent.
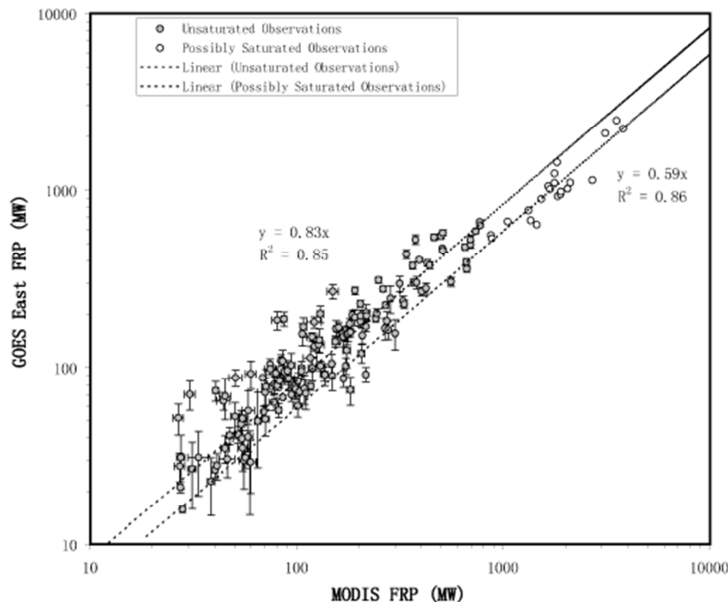

Figure 13: Intercomparison of the FRP of coincident fire clusters imaged by MODIS and GOES. Fire clusters were selected based on the criteria that the time difference was less than 10 mins and the MODIS scan angle less than 30 degrees. The comparison was divided into two groups, the first (146 matchup pairs) include fires where all GOES fire pixels in the cluster had MIR BT < 335 K (the specified saturation temperature of the sensor), and the second (22 matchup pairs) included fire clusters where one or more GOES fire pixels had MIR BT > 335 K. For the first group, the bias between GOES and MODIS is 22 MW, and the RMSE 66 MW.

Finally, estimates of FRE derived from the GOES FRP observations were converted to an estimate of fuel consumption using the default conversion factors of Wooster *et al.* (2005) and compared to the same measures contained in GFEDv2 (Figure 14). A reasonably good relationship is seen between the two measures, albeit one that appears to have some geographical variation. This confirms the FRP data from GOES as a strong source for real-time input into MACC. However, further work is necessary to deduce the source of the geographically varying scaling factor between the FRE- and GFED-derived fuel consumption estimates. Meanwhile, we are exploring possibilities to transition production of these GOES FRP data to the LSA SAF infrastructure within MACC II.
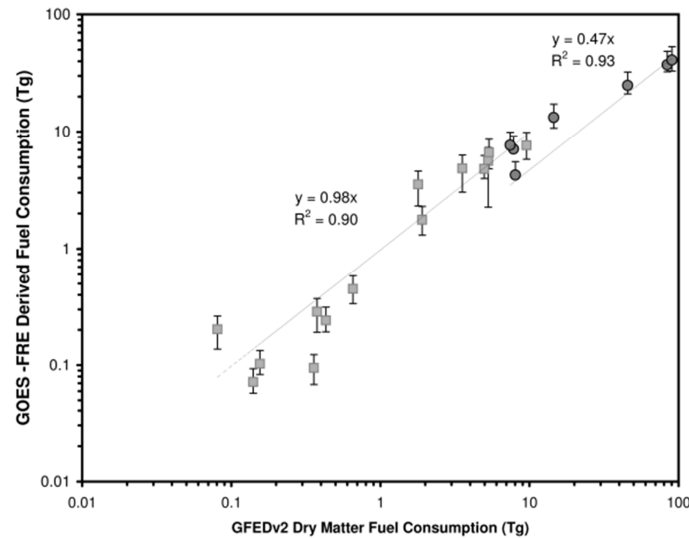
Figure 14: Comparison between the GOES-derived fuel consumption estimates calculated on an 8-day, 1-degree basis, and the same measure taken from the GFEDv2 Fire Emissions database of van der Werf et al. (2006). A strong relationship between these two independent fuel consumption estimates is clearly seen. The y-axis error bar indicates the difference between the cloud fraction normalized GOES-derived value, and the original non-cloud adjusted observations. Results from South America (closed circles) show a different relationship to those from Central/North America (closed squares).

2.1.4   SLSTR

D-FIRE is planning for the future use of active fire products within the GMES framework, since the current reliance on only MODIS as the polar orbiting data provider is unsustainable due to the already long lifetime of these NASA instruments (more than ten years for each of the two MODIS'). The dual-view Sentinel-3 Sea and Land Surface Temperature Radiometer (SLSTR) builds on the heritage of the (A)ATSR series of instruments, and the planned data products to be provided from SLSTR include an active fire (AF) detection and fire characterisation product aimed at supporting both operational Global Monitoring for Environment and Security (GMES) services and scientific applications having less stringent timeliness requirements. D-FIRE team members have influenced the design of Sentinel-3 SLSTR via specifying some of the characteristics of the wide dynamic range 'fire' channels, such that it will be more useful for active fire observations, and by specifying and testing a prototype active fire detection and FRP algorithm for this sensor (Wooster *et al.*, in press). The SLSTR will now have operation of the SWIR channels at night, and two low-gain middle IR and thermal IR spectral channels that are designed to minimise saturation over even high intensity fire events. Launch of the first Sentinel-3 satellite carrying SLSTR is expected in 2013/14, and operations (using four satellites in total) are expected to extend over a period of around 20 years. It is expected that SLSTR active fire data will feed directly into the D-FIRE system.

The SLSTR active fire detection algorithm works on a combination of data from the SLSTR near-nadir view visible and infrared spectral channels, and builds on previous 'hotspot' active fire detection algorithms developed for use with the ATSR, MODIS, BIRD HSRS, Meteosat SEVIRI and GOES Imager sensors. One significant adjustment compared to many current algorithms was the use of very relaxed 'potential fire pixel' thresholds, in order to attempt to make the algorithm relatively sensitive to even low FRP fire pixels. After a fire pixel has been confirmed as a fire by the detection stages of the

SLSTR algorithm, the pixels fire radiative power is calculated using the MIR radiance method of Wooster *et al.* (2003).

In the absence of real SLSTR imagery, SLSTR algorithm testing relied on using data from MODIS as the input data, since that instrument provides imagery across the full swath width planned for SLSTR in essentially the same spectral bands and at a very similar spatial resolution. In this way we were able to make a first evaluation of the new algorithms performance as compared to the existing MODIS fire detection algorithm used in version 5 of the MOD14 'MODIS Fire and Thermal Anomaly' Products (Giglio *et al.,* 2003) - which are those currently used within D-FIRE. Figure 15 and Figure 16 provide two examples of the algorithms application to MODIS imagery, and a visual comparison to the MOD14 fire detection performance, over regions of both 'large fire' and 'small fire' activity. We use high spatial resolution active fire detections from ASTER, made simultaneous with the Terra MODIS observations, to provide an independent accuracy assessment.
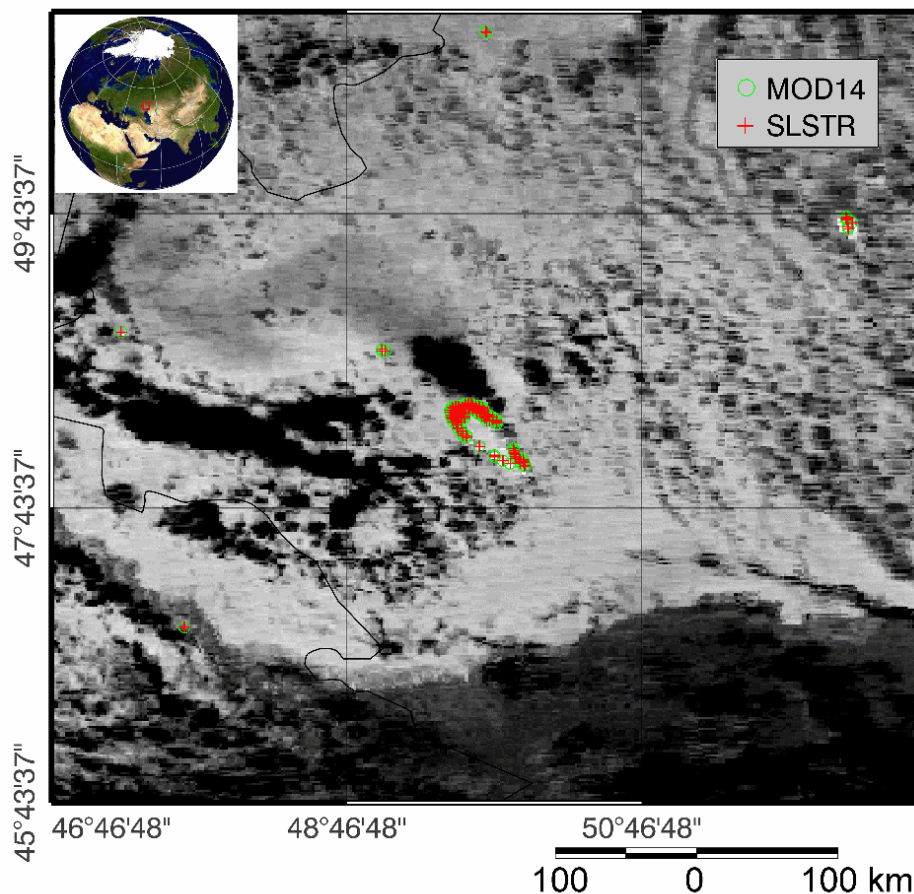
Figure 15: Daytime Aqua MODIS subscene of Kazakhstan, collected at 10:05 UTC on 1ˢᵗ June 2004. Background is the MIR channel image, in which cloud appears as black and which highlights active fire pixels as brighter than the surrounding background. The forest fire in the centre of this subscene represents what we believe to be one of the highest FRP fires imaged by MODIS (containing 108 fire pixels in all, and with a number of these having FRP > 1500 MW). Superimposed are the final set of confirmed active fire pixels detections made using the MOD14 (green circle) and the SLSTR (red cross) active fire detection algorithms. In this case the high intensity and large size of the fire results in an identical set of detections being made by the two algorithms. MODIS subscene coverage is indicated in the top left inset.

Figure 16: Daytime Terra MODIS $\Delta T_{MIR-TIR}$ scene of SE Africa collected at 08:20 UTC on 1st September 2001. Lakes Malawi and Tanganyika can be seen oriented N-S near the scene centre. Superimposed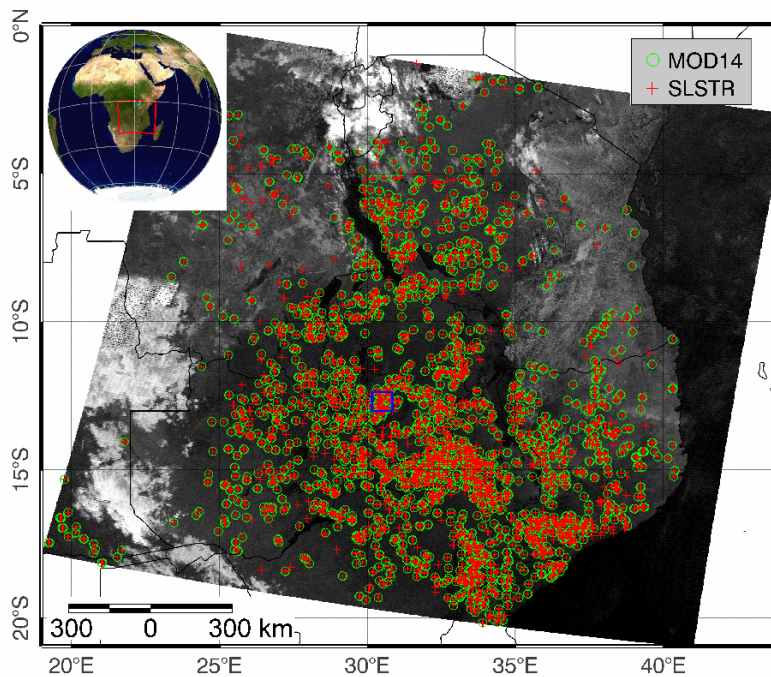 are the final confirmed fire pixels identified using the MOD14 (green circle) and the SLSTR (red cross) active fire detection algorithms. Many detections are common to both algorithms, but there are differences e.g. top left where the SLSTR algorithm identifies more active fire pixels than does the MOD14 algorithm. The area of the matching ASTER data acquisition is shown boxed in blue, just south of the scene centre. According to the GLC2000 landcover map, most of the detected fires are burning in shrublands / deciduous forest. MODIS scene coverage is indicated in the top left inset.

Using the combination of ASTER and MODIS imagery, it was determined that compared to clusters of fire pixels detected by ASTER, the SLSTR active fire detection algorithm shows an additional 1.2% commission ('false alarm') error on top of that shown by MOD14, but this was outweighed by a 4.2% reduction in omission ('missing fires') error. We also find that the SLSTR algorithm can apparently detect 13% more true fire clusters than can the MOD14 algorithm, at least in the MODIS scenes subject to testing. Of course, these statistics are only valid in the central part of the MODIS swath that matches the swath of ASTER, and at the overpass time of Terra MODIS (though this is expected to be very similar to that of SLSTR). Therefore the SLSTR algorithm appears to show some increased sensitivity to true fires compared to the current MOD14 algorithm, a fact directly related to its more liberal potential fire pixel detection thresholds. A true performance of the algorithm when applied to real SLSTR data must wait until launch of Sentinel-3 in ~2013/14, after which use of the data in D-FIRE will be developed.

2.2   Merged / Assimilated FRP Products

2.2.1   GFASv0

The global fire assimilation system (GFASv0) based on FRP observations by SEVIRI and MODIS has been run in real time throughout the MACC lifetime. The daily merged FRP field is generated by averaging all observations of fires (FRP>0) and all observations of no fire (FRP=0) with weights

according to fraction of the grid cell that has been observed (Kaiser et al. AIP 2009, ECMWF TM596 2009). This approach has been pioneered by MACC and adopted by several other systems since.

The processing is done on global grid with T159 resolution, i.e. about 1.1 deg. While GFASv0 corrects for partial cloud cover in a global grid cell, it does not fill observation gaps due to persistent cloud cover. Therefore, it contains vanishing values in all grid cells that have not been observed during the day.

The FRP map for 29 July 2010, which was produce in real time, is shown in the Figure 17. It clearly highlights the extreme fire event in European Russia along with an extreme fire episode in eastern Siberia and other fire seasons. The high observation frequency of SEVIRI leads to grid cells with very small daily average fire activity that is cause by short-lived fires. This effect is evident in Africa and Europe, where SEVIRI observations are used in GFASv0.
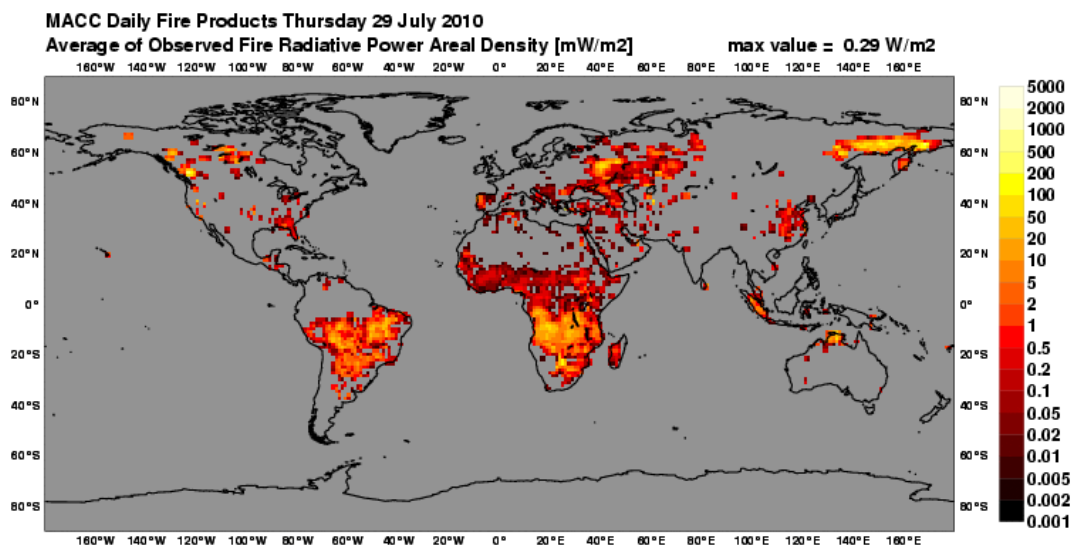
Figure 17: Merged FRP of GFASv0.

2.2.2 GFASv1

GFASv1 is a further development of GFASv0. Two versions are available that differ only in the resolution of the underlying global grid: 0.5 deg for GFASv1.0 and 0.1 deg for GFASv1.1. The improvements w.r.t. FRP processing over GFASv0 are:

- correction for duplicate observations due to bow-tie effect in the MODIS scan geometry

- automatic quality checking of the observation input

- masking of spurious FRP observations due to volcanoes, gas flares and other industrial activity

- observation gap filling with data assimilation using a Kalman filter

- higher spatial resolution

- full implementation in the operational infrastructure of ECMWF

The mask of spurious FRP observations has been generated with a statistical analysis of observed fire signal persistence and source identification of persistent signals (gas flaring, volcanoes, peat fires).

The errors of the assimilated daily global FRP analysis based on the observations by the two MODIS instruments are believed to be smaller than the remaining errors of the SEVIRI FRP observations after a simple bias correction. Therefore, the input of GFASv1 is limited to the MODIS observations and the latest work in D-FIRE has focused on a more sophisticated bias correction for the SEVIRI observations, see Sect. 2.1.2. Figure 18 shows the FRP analysis of GFASv1.0 for 29 July 2011, which has been published on 30 July 2011 on the MACC web site. Compared to the FRP field of GFASv0 published one year earlier and shown in Figure 17,

- the higher spatial resolution of GFASv1.0 is evident in the finer-scale features and the larger peak values of the field, and

- not including SEVIRI manifests itself in a lack of large areas with very small values in Africa and Europe.
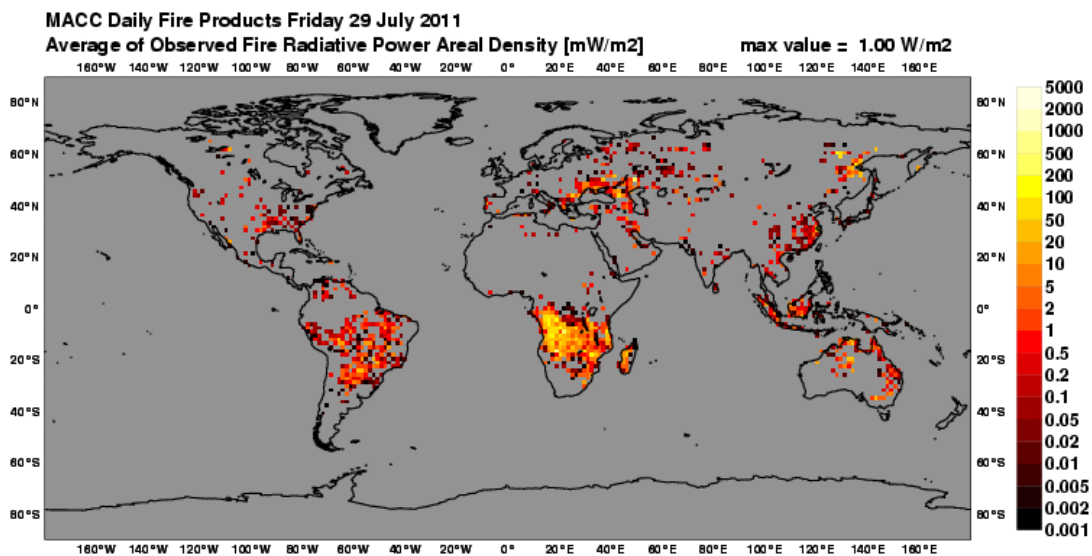
Figure 18: Assimilated FRP of GFASv1.0.

2.2.3   MACC reanalysis

In order to provide improved fire emission rates for the MACC reanalysis to G-IDAS, daily FRP fields have been calculated from the MODIS FRP products. In order to provide the best retrospective observation gap filling, the data assimilation of GFASv1 has been a modified into a Kalman smoother with a symmetric assimilation window of 5 days instead of the standard Kalman filter.

2.3   Emissions Products

2.3.1   GFASv0

In GFASv0, the dry matter combustion rate is calculated from the merged FRP with the universal conversion factor 1.37 kg/MJ (Kaiser et al. ECMWF TM596 2009). The emission rates of various species are subsequently calculated with land cover-specific emission factors from the literature, mostly Andreae & Merlet GBC 2001.

Emission rates for BC, CO2, CO, CH4, OC, PM2.5, SO2, TPM and C have been calculated since October 2008. NMHC and NOx are provided additionally since July 2010, following a user request.

The FRP-to-dry matter combustion rate conversion factor used in GFASv0 has been scaled so that the GFED2 CO emissions of previous years are matched. The value of 1.37 kg/MJ is much larger than the value of 0.368 kg/MJ that had been found in a laboratory study by Wooster et al. JGR 2005. This shows that such laboratory results cannot be applied straightforwardly to satellite data.

2.3.2   GFASv1

In GFASv1, the dry matter combustion rate is calculated from the assimilated daily FRP fields with eight land cover-specific conversion factors, which have been derived from linear regressions between the monthly assimilated FRP of GFASv1 and the dry matter combustion rates of GFEDv3.1. Within each land cover class, the correlation is sufficiently high to enable the reproduction of the GFED combustion rate from the GFAS FRP within in the accuracy of GFED (Heil et al. ECMWF TM628 2010). The consistency is illustrated in Figure 19. It also shows that GFAS has a lower detection threshold than GFED. GFASv1 is therefore a combined system that incorporated information from GFED and the FRP observations in real time.

The land cover map has been specifically developed by D-FIRE for the purpose of deriving dry matter combustion rate from FRP observations. It is based on the historical dominant fire type distribution in GFEDv3.1 and an additional peat map of Russia. The map is also used for the selection of the assignment of the appropriate emission factors for the species emission calculation.

The land cover-specific emission factor compilation of GFASv0 has been updated with recent literature and extended to comprise all species that are need in the MACC aerosol, greenhouse gas, and reactive gas models. The following species are included: BC, CO2, CO, CH4, OC, PM2.5, SO2, TPM, C, H, NOx, N2O, NMHC, C2H4, C2H4O, C2H5OH, C2H6, C2H6S, C3H6, C3H6O, C3H8, C5H8, CH2O, CH3OH, Higher_Alkanes, Higher_Alkenes, NH3, Terpenes, Toluene_lump, C7H8, C6H6, C8H10, C4H8, C5H10, C6H12, C8H16, C4H10, C5H12, C6H14, C7H16.

Two parallel system, v1.0 and v1.1, produce these fire emissions at different resolutions of 0.5 deg and 0.1 deg. Figure 20 shows a comparison of continental scale daily budgets of the CO emissions in GFASv1.1 and v1.0 since 7 Feb 2011. It shows that v1.1 produces on average 5% more emissions than v1.0. The individual continental scale budgets are larger by 2% - 12%. The temporal behaviours of the two versions are very similar with occasional outliers. The differences indicate that the cloud cover correction and observation gap filling of GFAS have some dependency on resolution.
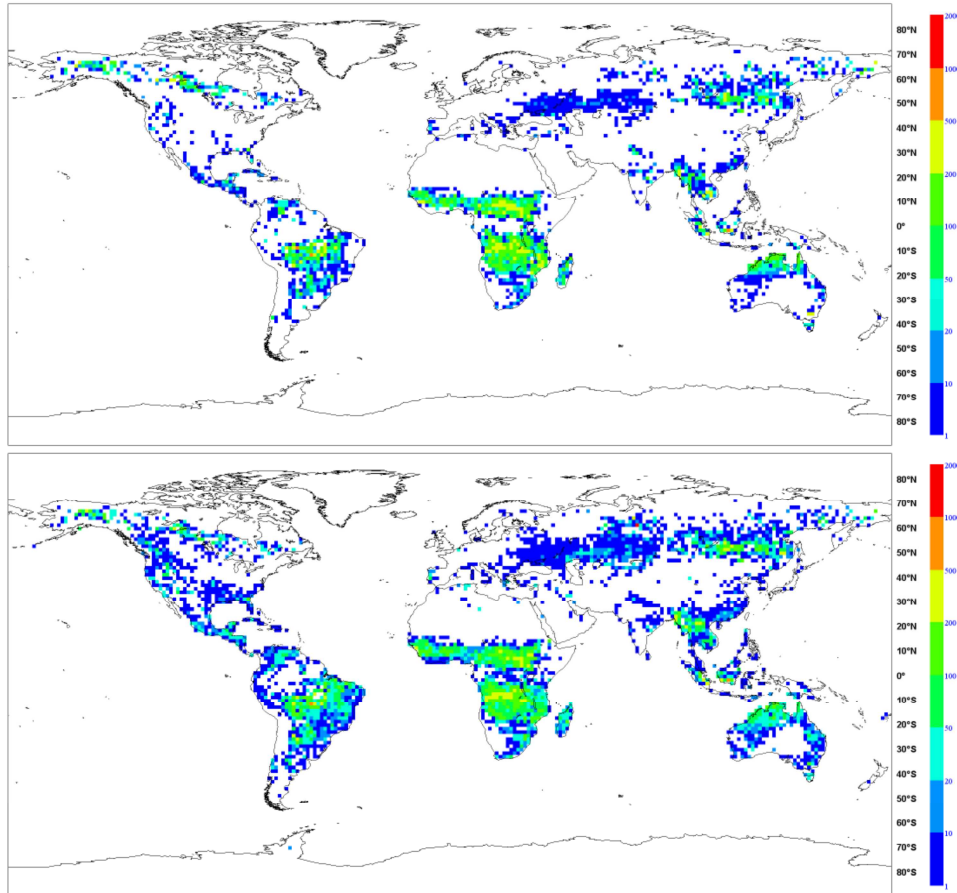
Figure 19: Average distribution of carbon combustion [g/a/m2] during 2003-2008 in GFED3.1 (top) and GFASv1.0 (bottom). (Kaiser et al. BG 2012)
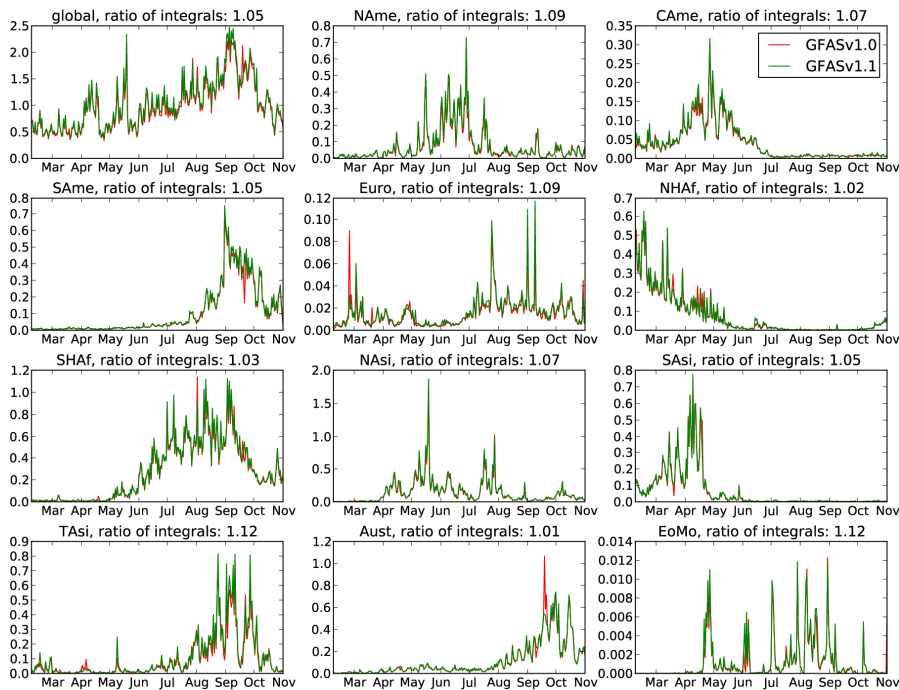

Figure 20: Daily CO emissions of GFAS v1.0 and v1.1 at continental scale in 2011. Region definitions according to Kaiser et al. BG 2012.

2.3.3 GFEDv3.1

The update of GFED from version 2 to version 3 was finalized in MACC and the data were released for use in MACC and other projects. The public GFED3 database is also labelled "GFEDv3.1" in order to distinguish it from a preliminary version "GFEDv3.0" that has also been used in MACC. The two papers describing the GFED3 approach to estimate burned area and emissions were published [Giglio et al. 2009, van der Werf et al. 2010]. In addition, the GFED3 framework calculates biosphere CO2 fluxes (NPP and heterotrophic respiration), which have been shared with D-GHG for use as a-priori input.

GFED3 is based on burned area derived from MODIS. This is a major departure from the GFED2 approach, where active fires were scaled to a limited set of burned area. While this approach is still used in several areas / years where burned area was not available, about 90% of the global burned area from 2001 through 2009 was based on mapped burned area. Burned area is converted to emissions using the same modelling framework as in GFED2, but has undergone a number of changes outlined below.

The spatial resolution has increased from 1 to 0.5 degree. The native resolution 500-meter maps of burned area have been used to assess what the contributions of different types of fires were to the total 0.5 degree emissions estimates. This allowed for an improved representation of spatial and temporal variability in fuel type burning and mortality rates, and the ability to better apply emission factors

The leaf senescence scalar has been improved to reduce carry-over of leaves during the dry season to the following wet season in herbaceous vegetation types. This decreased biomass in herbaceous fuels, more in line with measurements.

The NPP allocation has been changed from a fixed to a dynamic allocation based on mean annual precipitation. This allowed for a better representation of spatial variability in aboveground biomass in highly productive ecosystems.

The emissions are partitioned into different categories depending on fire type. They include deforestation fires, savannah fires, agricultural waste burning, peat fires, and forest fires. This partitioning enables better application of emission factors which relate dry matter consumption to emissions of trace gases and aerosols.

The list of species for which emissions are estimated has been extended to cover all the required species for MACC, i.e. BC, CO2, CO, CH4, OC, PM2.5, SO2, TPM, C, H, NOx, N2O, NMHC, total carbon emission, C2H4, C2H4O, C2H5OH, C2H6, C2H6S, C3H6, C3H6O, C3H8, C5H8, CH2O, CH3OH, Higher_Alkanes, Higher_Alkenes, NH3, Terpenes, Toluene_lump.

An overview of average global emissions estimates and differences between GFED3 and GFED2 are shown in Figure 21 and Figure 22. The large-scale spatial distribution of fire emissions in GFED3 is not that different from GFED2, but due to the stronger reliance on burned area the differences on smaller scales are substantial.

An uncertainty estimate has also been included in GFED3. Uncertainties remain substantial, even with the improved burned area estimates. On annual, continental scales these are in the order of 20% (1 sigma), but can increase to much higher values in areas where organic soil burns, areas where no burned area estimates are available and where we had to revert to relations between fire hot spots and burned area, and in deforestation areas.
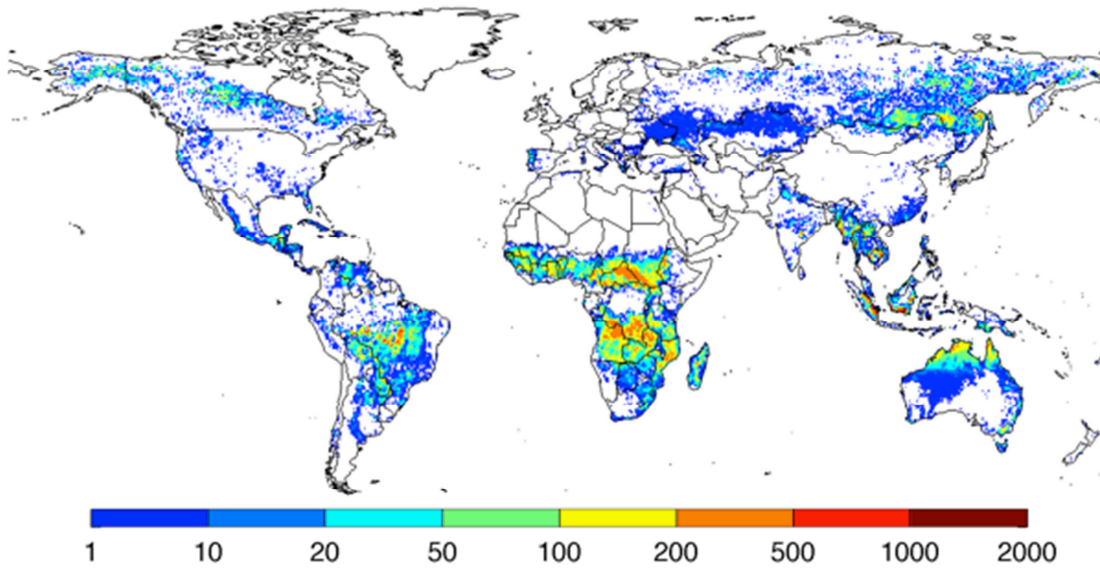
Figure 21: Mean annual fire carbon emissions (g C m-2 yr−1) in GFEDv3.1, averaged over 1997–2009.
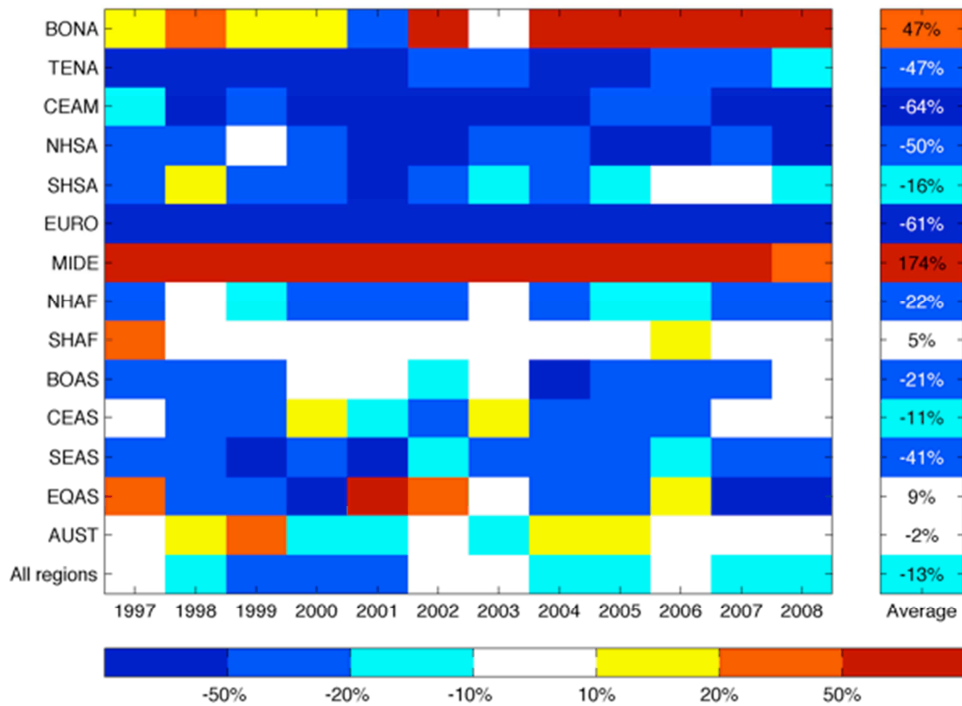
Figure 22: Differences in fire CO emissions estimates between GFED3 and GFED2, as a percent of GFED2 estimates. Positive numbers indicate GFED3 is higher than GFED2 and vice versa. For region abbreviations please see van der Werf et al. ACP 2010. Note that emissions in MIDE (Middle East) are negligible on a global scale.

The GFED3 data publicly available as web download in ASCII format. It has also been stored in GRIB format in MARS to provide access in a format that is consistent with GFAS.

2.3.4   GFEDv3.0

Since the production of the MACC reanalysis started before GFED3 was finalised, a near-final version, GFEDv3.0, was produced for use in the MACC reanalysis.

The differences between GFEDv3.0 and GFEDv3.1/GFED3 mostly include final tuning of parameters to match most recent literature and the use of the most recent burned area estimates. The parameters that changed were mostly depth of burning in tropical peatlands and organic soils in boreal regions. In addition, the algorithm that combines burned area and active fire detections to estimate deforestation rates was revised.

In the description of changes below we focus on carbon emissions, but changes in emissions of traces gases are comparable as the changes made to the emission factors that convert carbon (or dry matter) emissions to emissions of trace gases and aerosols were minimal.

In almost all regions emissions increased from version 3.0 to 3.1, except in the tropical deforestation zones, see Table 2 and Table 3. The increase was on average 9% over the 1997-2008 period on a global scale. Regionally, the increases were highest in areas with emissions due to the burning of organic soils, such as the boreal region and Indonesia. Here the increases in depth of burning translated directly to higher emissions. The largest decrease occurred in South America, while in equatorial Asia lower emissions from fires used in the deforestation process were offset by increased emissions from peatlands.

Figure 23 shows that the differences increased along a South-North gradient in the boreal zone, coinciding with the increasing role of belowground fuels compared to aboveground fuels. This is most obvious when focusing on the relative changes (Figure 23, bottom panel); in absolute terms these tundra regions contribute relative little to the boreal fire emissions.

The decreases are most evident in the so-called 'arc of deforestation' in Brazil, Bolivia, and Peru. Here most fire-driven deforestation takes place and the role of other types of fires is relatively modest, so any change in burned area associated with deforestation will translate directly to regional fire emission estimates.

In summary, several changes have been made to the GFED modelling framework when updating version 3.0 to 3.1. These changes included the use of the most recent burned area estimates, revised estimates of fire-driven deforestation rates, and revised estimates of the depth of burning in organic soils. The global total increased by 9% but on regional scales the differences are larger, and in some grid cells differences exceeded 50%.

	1997	1998	1999	2000	2001	2002	2003	2004	2005	2006	2007	2008	Mean
													GFED3.0
Boreal North America	15	100	25	10	6	70	60	99	51	47	33	42	**46**
Temperate North America	2	9	13	14	6	12	9	4	6	10	16	11	**9**
Central America	13	65	15	27	10	14	30	9	27	22	16	17	**22**
Northern hemisphere South America	27	45	15	19	18	10	61	33	14	12	28	15	**25**
Southern hemisphere South America	201	517	369	141	174	252	251	352	481	241	530	191	**308**
Europe	4	5	3	9	6	2	5	2	4	4	6	2	**4**
Middle East	1	2	2	1	2	2	1	1	1	2	2	1	**2**
Northern hemisphere Africa	509	533	477	484	392	447	457	366	488	406	409	401	**447**
Southern Hemisphere Africa	427	599	459	446	475	453	545	525	572	512	499	530	**503**
Boreal Asia	40	277	78	108	63	150	234	17	34	77	37	131	**104**
Temperate Asia	33	22	15	21	34	40	25	24	25	27	27	32	**27**
Southeast Asia	45	136	114	38	38	80	61	134	76	94	143	56	**85**
Equatorial Asia	916	164	26	13	64	263	64	97	115	302	23	21	**172**
Australia & New Zealand	117	111	189	135	179	146	120	145	84	140	116	75	**130**
Global total	2352	2587	1801	1467	1468	1943	1924	1809	1980	1897	1888	1527	**1887**
													GFED3.1
Boreal North America	19	116	36	14	5	69	60	139	66	50	40	49	**55**
Temperate North America	2	8	11	12	6	10	9	4	6	11	20	13	**9**
Central America	14	60	14	27	9	13	28	8	27	20	14	14	**21**
Northern hemisphere South America	20	51	14	19	17	9	54	26	13	11	25	13	**23**
Southern hemisphere South America	201	412	298	137	143	231	214	327	459	241	572	194	**286**
Europe	4	6	3	9	5	2	5	3	5	4	7	2	**5**
Middle East	1	2	2	1	2	2	2	2	1	2	3	1	**2**
Northern hemisphere Africa	581	586	511	532	428	479	506	407	532	442	441	445	**491**
Southern Hemisphere Africa	514	682	534	514	514	483	597	579	621	548	533	578	**558**
Boreal Asia	42	338	85	141	103	191	333	16	48	96	46	165	**134**
Temperate Asia	57	31	18	37	33	49	43	25	27	35	35	40	**36**
Southeast Asia	65	187	160	56	40	91	69	166	87	83	165	64	**103**
Equatorial Asia	1069	184	33	21	70	285	71	109	123	368	21	25	**198**
Australia & New Zealand	118	112	182	146	186	153	128	155	89	147	122	78	**135**
Global total	2707	2778	1901	1665	1561	2067	2119	1967	2105	2060	2044	1681	**2055**

Table 2: Carbon emissions (Tg C year-1) for GFED3.0 and 3.1 for 14 basis regions and the global total for 1997-2008

	1997	1998	1999	2000	2001	2002	2003	2004	2005	2006	2007	2008	Mean
GFED3.1 – GFED3.0 (Tg C year-1)													
Boreal North America	3	16	11	4	-2	-1	0	41	15	3	7	7	9
Temperate North America	0	-1	-2	-2	0	-2	0	0	0	1	3	2	0
Central America	1	-4	-2	0	-1	-1	-2	-1	0	-2	-2	-3	-1
Northern hemisphere South America	-7	6	0	0	-1	-1	-8	-7	-2	-2	-3	-2	-2
Southern hemisphere South America	0	-104	-71	-4	-32	-21	-37	-25	-23	0	42	3	-23
Europe	0	1	0	0	-1	0	0	0	1	1	0	0	0
Middle East	0	0	0	0	0	0	0	0	0	0	0	0	0
Northern hemisphere Africa	72	53	34	48	36	32	49	41	45	36	31	44	43
Southern Hemisphere Africa	87	83	75	68	40	30	52	54	50	37	35	48	55
Boreal Asia	1	61	7	33	41	40	99	0	13	20	9	34	30
Temperate Asia	24	10	2	16	-1	8	18	1	2	8	9	8	9
Southeast Asia	20	51	46	17	2	11	8	32	11	-11	21	8	18
Equatorial Asia	153	20	7	8	6	22	8	11	8	65	-2	3	26
Australia & New Zealand	2	1	-6	11	7	6	8	10	4	7	6	3	5
Global total	355	191	100	198	93	124	195	158	125	163	156	155	168
GFED3.1 – GFED3.0 (%)													
Boreal North America	23	16	46	37	-26	-1	0	41	30	7	20	16	19
Temperate North America	-11	-8	-16	-16	-6	-15	1	8	-2	9	20	17	-1
Central America	6	-7	-10	0	-10	-7	-7	-9	0	-10	-13	-19	-7
Northern hemisphere South America	-26	12	-3	-1	-8	-10	-13	-21	-11	-14	-12	-11	-9
Southern hemisphere South America	0	-20	-19	-3	-18	-8	-15	-7	-5	0	8	2	-7
Europe	6	11	-4	-2	-9	-6	9	11	22	15	7	-10	4
Middle East	1	-1	2	7	3	0	6	8	7	13	20	8	6
Northern hemisphere Africa	14	10	7	10	9	7	11	11	9	9	8	11	10
Southern Hemisphere Africa	20	14	16	15	8	7	10	10	9	7	7	9	11
Boreal Asia	4	22	9	30	65	27	42	-2	40	26	23	26	29
Temperate Asia	73	45	15	77	-4	21	73	6	9	31	33	27	33
Southeast Asia	44	38	41	45	7	14	13	24	15	-11	15	14	21
Equatorial Asia	17	12	25	58	10	8	12	12	7	22	-7	15	15
Australia & New Zealand	1	1	-3	8	4	4	6	7	5	5	5	4	4
Global total	15	7	6	13	6	6	10	9	6	9	8	10	9

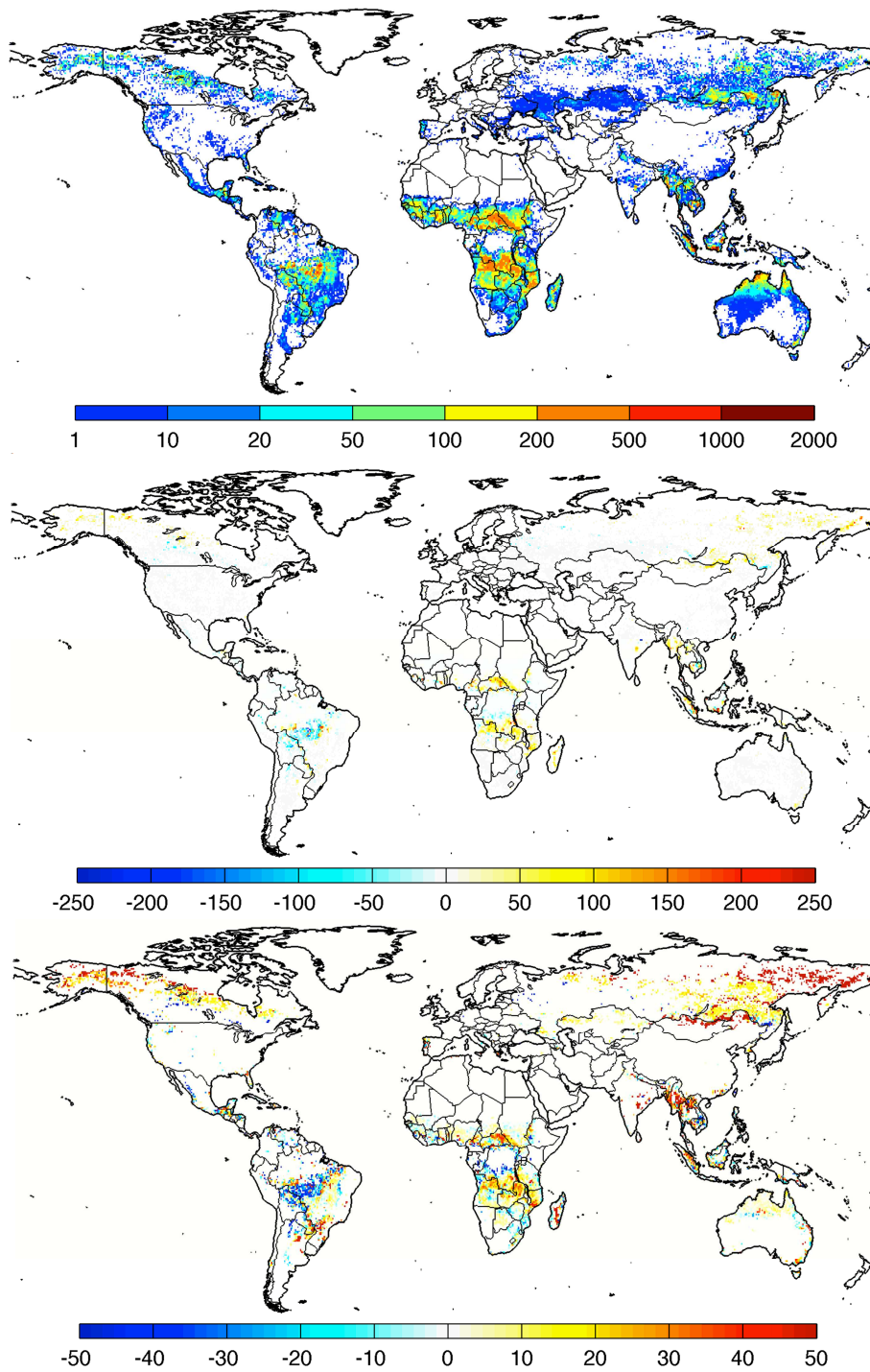*Table 3: Difference between GFED3.0 and 3.1, both as absolute values (Tg C year-1) and as percentage*

Figure 23: Annual average carbon emissions (1997-2008) in Tg C year-1 according to GFED3.1(top), absolute difference with GFED3.0 (middle), and relative difference with GFED3.0 in percentage (bottom).

2.3.5   MACC reanalysis

The fire emissions in the GEMS reanalysis have been based on the GFEDv2 inventory. For the MACC reanalysis (Inness et al. ACP 2013), D-FIRE has compiled an improved inventory from the GFEDv3.0 inventory and MODIS FRP observation processed in GFAS. Since GFEDv3.1 was not yet finalised at the start of the MACC reanalysis, GFEDv3.0 was created specifically for the MACC reanalysis, see Sect. 2.3.4. The monthly emissions GFEDv3.0 were subsequently redistributed in each 0.5 deg grid cell and on all days of the month according to daily 0.1 deg FRP distribution generate by GFAS from MODIS observations, see Sect. 2.2.3. Thus a higher resolution dataset with the GFEDv3.0 budgets was obtained. The redistribution of the monthly GFED emissions into daily emissions is illustrated in Figure 24.
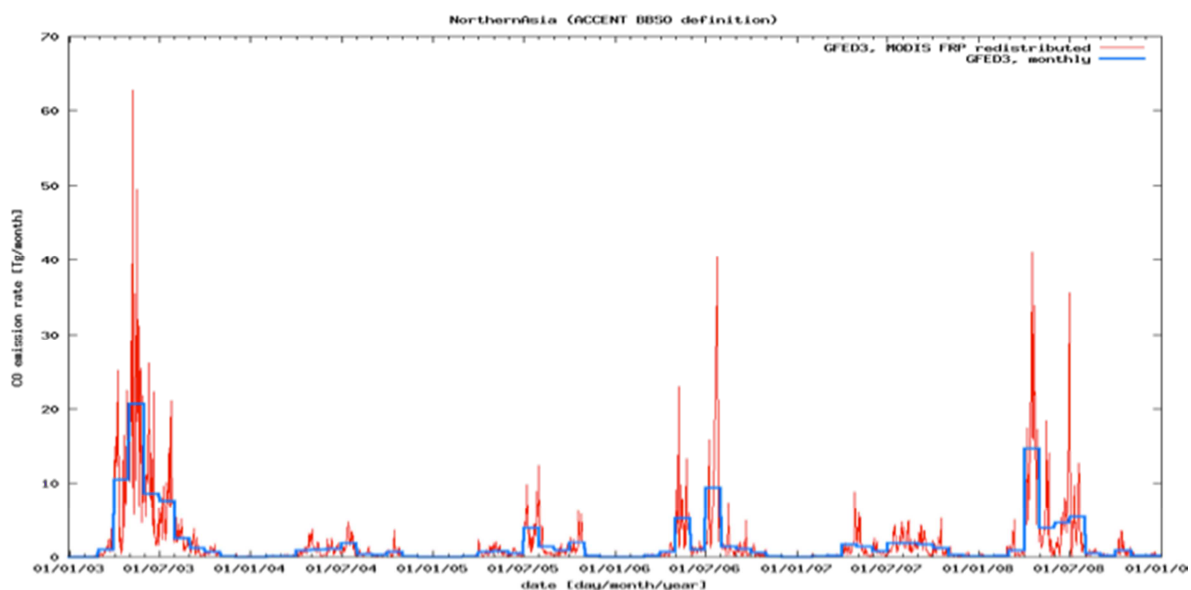
Figure 24: CO emission rate over Northern Asia for 2003-2008 in GFEDv3.0 (blue) and the D-FIRE reanalysis product (red).

Thus the fire emission in the MACC reanalysis of 2003-2008 differ from those in the GEMS reanalysis in the following aspects:

- GFED version 3.0, instead of version 2

- temporal resolution of 1 day instead of 8 days

- spatial resolution of 0.1 deg instead of 1 deg, based on our MODIS FRP time series

- extended list of species: BC, CO_2, CO, CH_4, OC, PM2.5, SO_2, TPM, C, H, NOx, N_2O, NMHC, total carbon emission, C_2H_4, C_2H_4O, C_2H_5OH, C_2H_6, C_2H_6S, C_3H_6, C_3H_6O, C_3H_8, C_5H_8, CH_2O, CH_3OH, Higher_Alkanes, Higher_Alkenes, NH_3, Terpenes, Toluene_lump.

During the production of the reanalysis of 2009 and 2010, the daily GFASv1.0 emissions were available and used. GFASv1.0 is a effectively consistent extension of the 2003-2008 time series based on GFEDv3.0 and MODIS FRP because it was designed to be consistent with GFEDv3.1 and to have a daily time resolution.

3 GFASv1 Applications and Validation

The GFAS emission products have been used in various services of MACC throughout the project duration. Since GFASv1 has been designed to be consistent with GFEDv3.1, one cannot be used as independent validation of the other. Therefore, the main focus of the validation has been the feedback from atmospheric applications in MACC. Additional validation has been performed by comparisons with NASA's fire emission product and with independent flux inversions.

3.1 Applications in the MACC services

As described in Section 0, the emissions from GFEDv3.0, assimilated MODIS FRP and GFASv1.0 have been used in the MACC reanalysis for reactive gases, greenhouse gases and aerosols.

The GFASv0 emissions of aerosols and greenhouse gases have been used in the real time and delayed mode global analysis and forecasting services starting from the beginning of MACC. After GFASv1.0 became available in 2011, the systems switched to GFASv1.0 and an enhancement factor for aerosols was introduced, cf. Sect. 3.2.

The campaign support service with CO tracer forecasts has used GFASv0 emission throughout the MACC period. Use of the GFASv1.0 emissions in the global reactive gas forecasts with IFS-MOZART and IFS-TM5 has been tested successfully in several off-line studies. It is now being implemented in the upcoming real time service for reactive gas analysis and forecasting.

3.2 Validation of aerosol emissions

The magnitude of the aerosol emissions in GFASv1.0 has been validated by several global and regional comparisons. This involved close collaboration with the MACC global aerosol sub-project and external scientists.

3.2.1 Global MODIS AOD observations

Kaiser et al. BG 2012 use the AOD of organic matter (OM) and black carbon (BC) in an MODIS AOD-constrained analysis of the global MACC aerosol system as continuous representation of the MODIS AOD observations. In is compared to the smoke AOD in a 6-month model simulation that is driven by GFASv1.0 emissions. An average underestimation by a factor of 3.4 is found for the 6-month study period. Consequently, an enhancement of the aerosol emissions by a factor of 3.4 when used in the current global MACC service is recommend and implemented. Further studies have started. Figure 25 shows an extension of the comparison to almost a full year. It results in a recommended enhancement factor of 3.3, which is consistent with the original recommendation of 3.4. It also shows that the limitations of this study approach: The global background value of OM and BC is higher in the analysis than in the enhanced model forecast and the peak values are, correspondingly, lower. Furthermore, anthropogenic OM and BC emissions in Asia introduce errors. Therefore, a more detailed parameter study is need in the future.
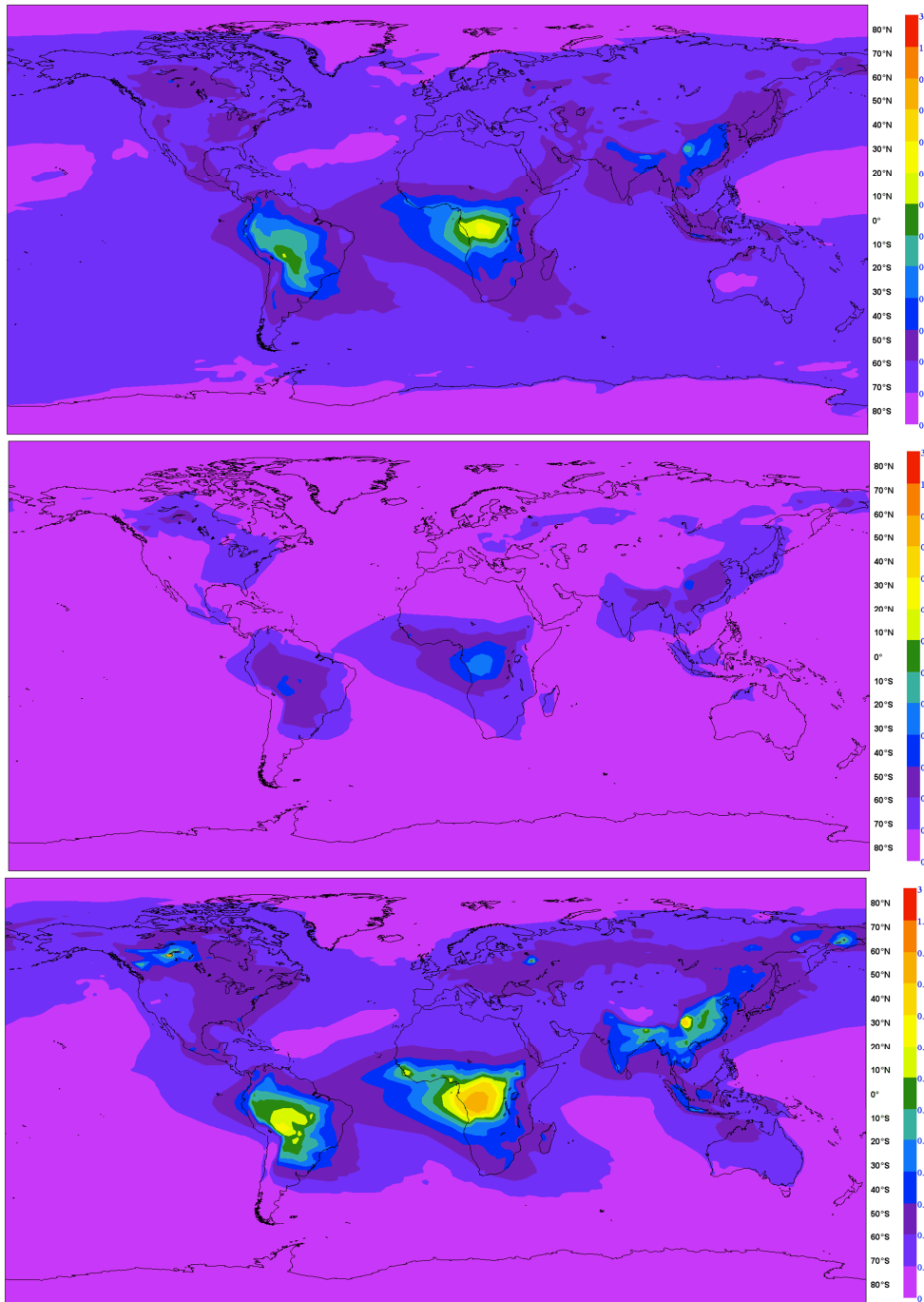
Figure 25: Average AOD of organic matter and black carbon for 1 Jul 2010 - 18 Jun 2011 in the observation-constrained analysis (top), forecast (middle), forcast enhanced by factor 3.3 (bottom)

3.2.2   Independent global bottom-up inventory

The black carbon (BC) emissions of GFASv1.0 have been compared to those of the GFED emission monitoring system developed by NASA. GFED is an independent system from GFAS but based on the same observational input, i.e. MODIS FRP. Several scaling parameters in QFED_v2.2 have been tuned to achieve consistency of NASA's GEOS5 model with QFED emissions and the MODIS AOD observations. A comparison to GFEDv3.1 is also included in the comparison. GFED and QFED are completely independent. The "GFAS_v1.e" data in Figure 27 and Figure 28 refer to the GFASv1.0 emissions enhanced by a factor of 3.4. The comparison confirms the agreement between GFASv1.0 and GFEDv3.1. It also shown a good agreement between the MODIS AOD-tuned emission estimates GFASv1.0 with aerosol enhancement factor and QFEDv2.2. This indicates that the enhanced aerosol emissions are not only appropriate for the MACC system but also for other global models. The comparison also confirms the regional and temporal distribution of the GFASv1.0 emissions.
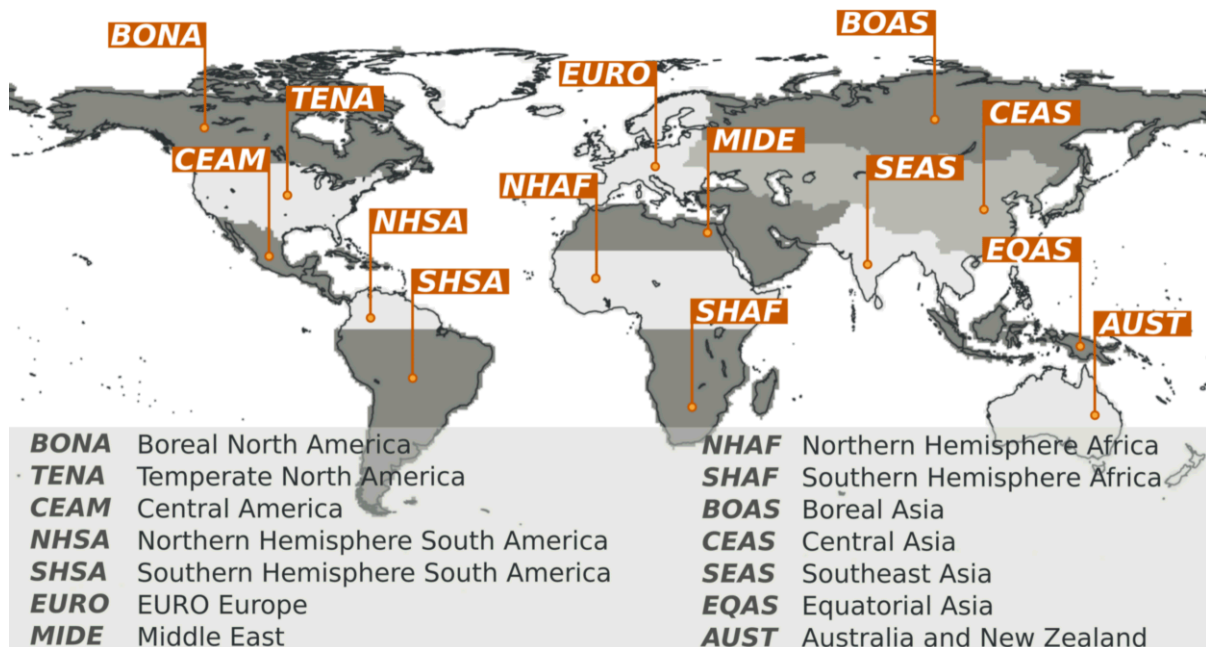

Figure 26: Definition of regions for comparison to GFED. (courtesy A. da Silva, NASA)
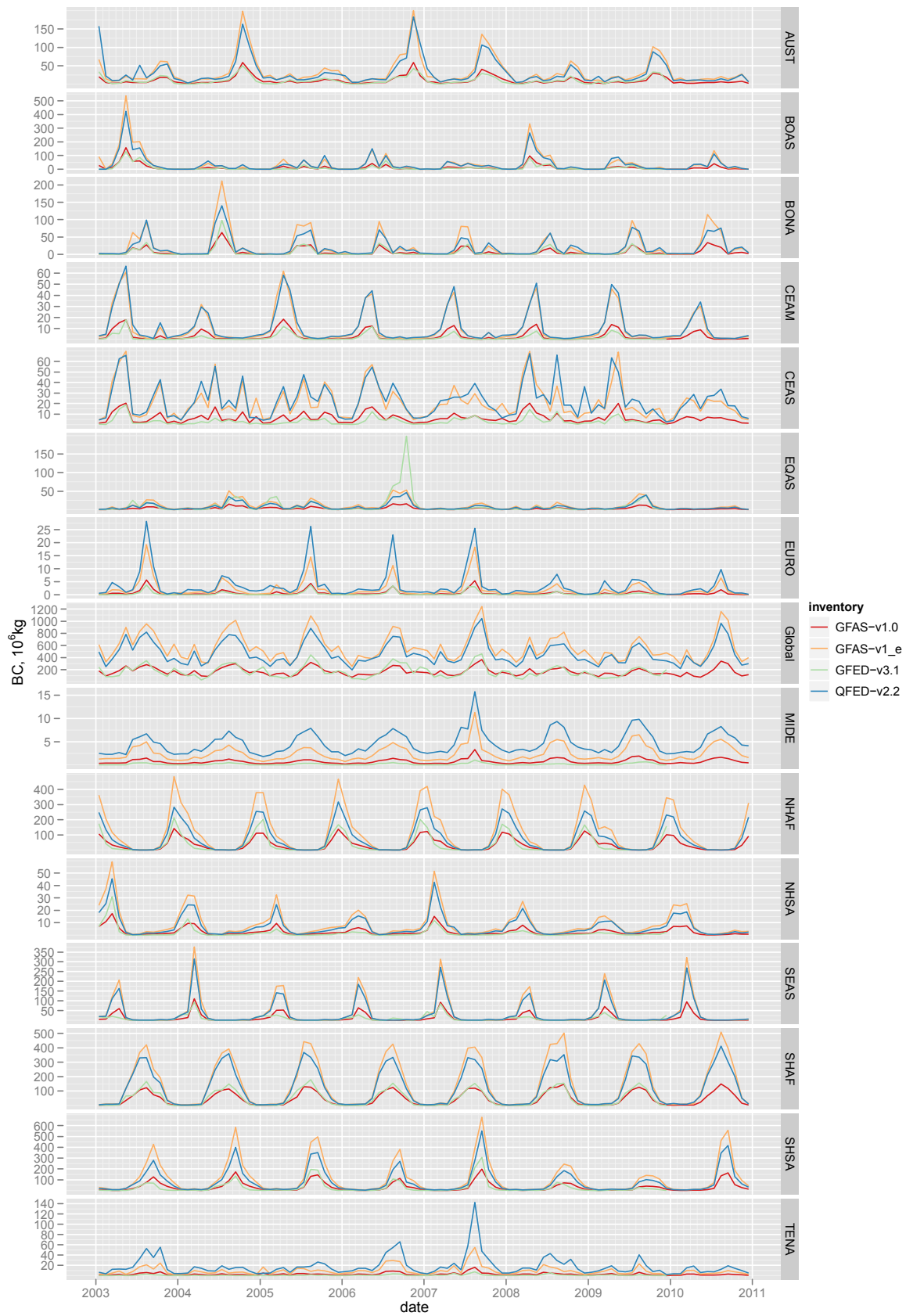
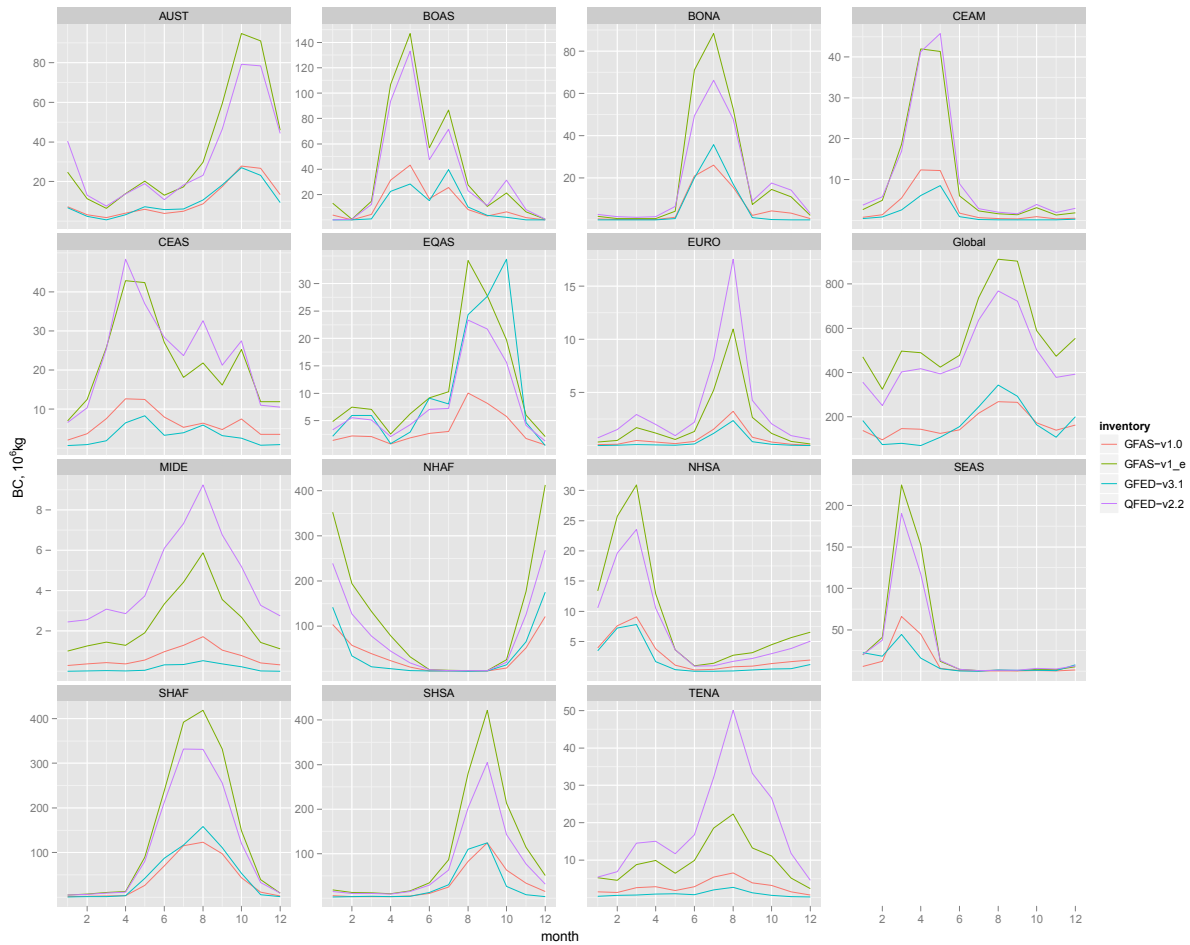*Figure 27: Comparison to GFED time series. (courtesy A. da Silva, NASA)*

Figure 28: Comparison to GFED seasonal cycle. (courtesy A. da Silva)

3.2.3   Independent global source inversion

Huneeus et al. ACPD 2011 have conducted a global aerosol source inversion that is independent of the global MACC systems. They conclude that biomass burning has emitted 96 Tg of smoke aerosols per year during their study period. This is in excellent agreement with the enhanced GFASv1.0 estimate of 99 Tg/a and confirms again that the enhanced value is appropriate for use in global atmospheric aerosol models.

3.2.4   Local AERONET observations: Russian fires of 2010

Following anomalously high temperatures, large wildfires devastated parts of Russia to the east of Moscow in July and August 2010. Because of the dry conditions, peaty soil fires developed, which emitted large quantities of smoke. The thermal radiation of the fires and the aerosol optical depth of the smoke were observed by NASA's MODIS instruments and used in the global real time forecasting system of MACC. Figure 29 shows the distributions of fires on 4 August and of smoke on 8 August as represented in the global real time service of MACC. The time series of in-situ observations of PM10 in the lower panels show that the air quality of Virolahti in Finland was affected by smoke around 8 August, which caused a transgression of the EU threshold of 50 μg(PM10) m-2 for the 24-hour average. The 1-day and 3-day forecasts of PM10 at Virolahti that were produced by MACC's global aerosol forecasting system match the in-situ observations well, thus highlighting the ability of MACC to monitor and forecast the global distribution of aerosols with an accuracy that allows local air quality

applications. The excellent accuracy is primarily attributed to the combination of data assimilation of aerosol optical depth observations with the accurate representation of atmospheric transport in the IFS.
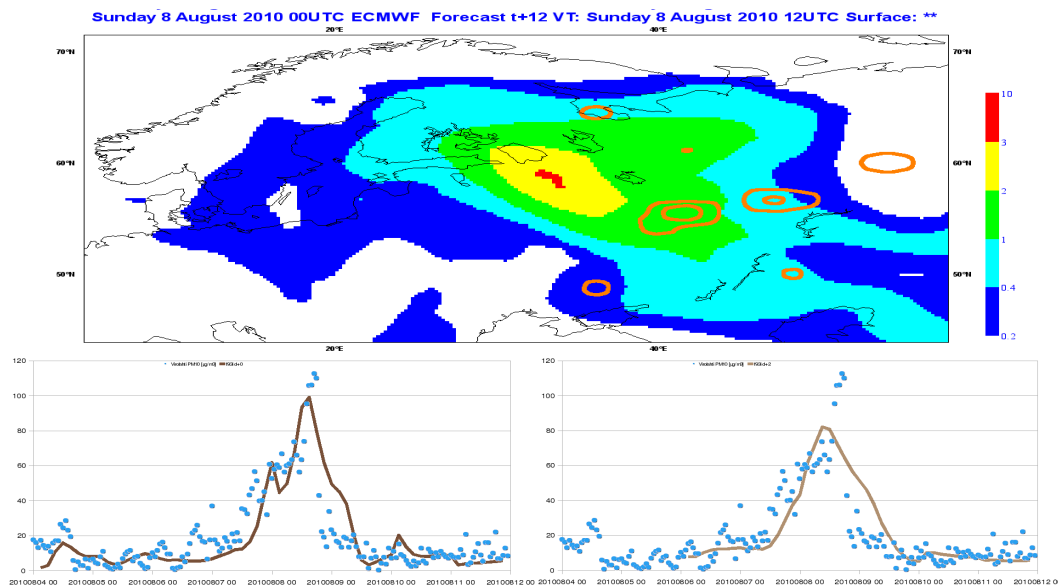

Figure 29: Smoke and fires in Russia in summer 2010 as represented in the global MACC system: The upper panel shows the aerosol optical depth of anthropogenic aerosols in the 1-day forecast extending to Finland on 8 August 2010 (colour-coded) and the observed fires four days before (contour lines at 50 and 500 mW m-2 fire radiative power). PM10 observations at Virolahti in Finland (lower panel, symbols, courtesy FMI) confirm the passing through of smoke and an air quality threshold transgression predicted by the 1- and even 3-day forecasts of MACC (lines, left and right). All data were produced in real time. [Kaiser et al., ESA SP-688, 2010]

MACC answered the French Ministry of Ecology query concerning forecasts of the Russian smoke plume forecasts by showing that the ECMWF member states, except Finland, would be hardly affected by the smoke. MACC also published a news item on its web server that listed its products providing information on the Russian fires and smoke.

The space-borne fire observations used in MACC show that the diurnal cycle of the fires was flat, which is in sharp contrast to that of previous years' fires, which virtually extinguished at night, cf. Figure 30. Thus the type of the Russian fires in summer 2010 can be characterised as "peaty soil fire", while the static land cover map of GFEDv2, which is used in GFASv0, classifies the region as "non-tropical forest". This discrepancy and the strong underestimation of the FRP in the SEVIRI product have together led to severe underestimation of the fire emissions in the real time products of GFASv0 even though the location and temporal evolution of the emissions were shown to be consistent with atmospheric plume observations. This shortcoming has been addressed in GFFASv1.0 by (1) developing a dedicated land cover map that also includes information from Russian peat maps, (2) deriving and utilising land cover-specific conversion factors for the calculation of dry matter combustion rate, and (3) blacklisting of SEVIRI FRP products (Kaiser et al. BG 2012). 1-day hindcasts of the aerosols in Moscow and independent AOD observations by AERONET are shown in Figure 31. The good agreement of the hindcast simulation "GFAS", which is based on factor-3.4 enhanced GFASv1.0 emissions and has no atmospheric AOD assimilation, with the AERONET

observations shows that the globally derived aerosol enhancement factor is also applicable for individual events and confirms the budget and the temporal and spatial variability of the aerosol emissions in GFASv1.0. The different distributions of the aerosol types in the four simulations shows that even the assimilation of MODIS AOD critically depends on accurate fire emissions for a realistic partitioning of the aerosol types. A detailed discussion can be found in Huijnene et al. ACP 2012.
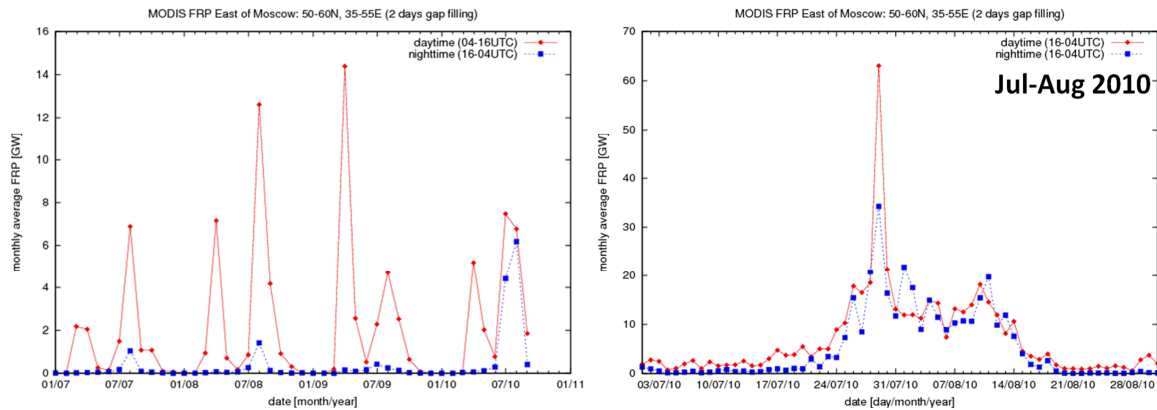

Figure 30: FRP observed during daytime (red) and night-time (blue) east of Moscow. Monthly values are shown for 2007–2010 (left). Daily values are shown for July and August 2010 (right). [Kaiser et al., ESA SP-688, 2010]
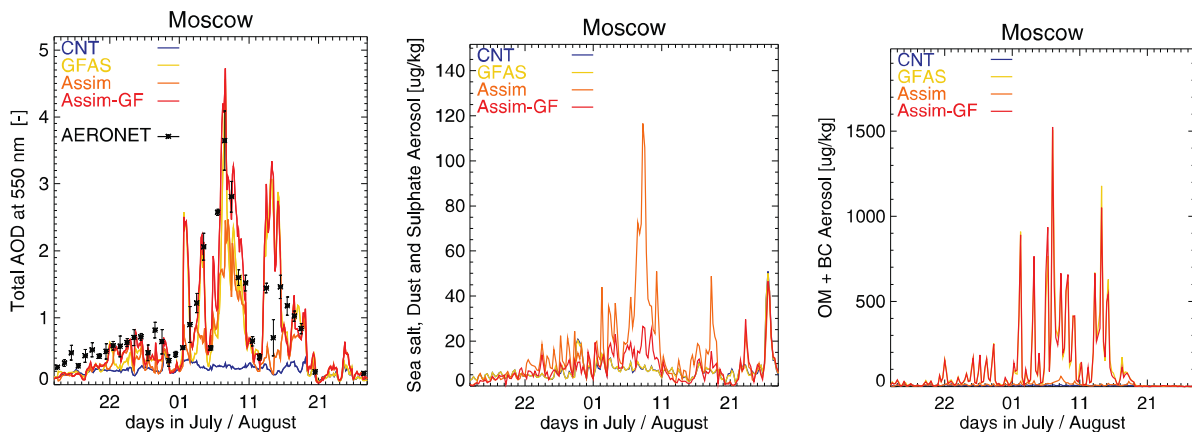

Figure 31: AOD in Moscow during July/August 2010. AERONET observations and MACC global aerosol model simulations (CNT, GFAS) and analysis (Assim, Assim-GF) driven by climatological emissions (CNT, Assim) and enhanced GFASv1.0 emissions (GFAS, Assim-GF). (Huijnene et al. ACP 2012)

3.2.5   Validation of reactive gas emissions

The validation of the reactive gas emissions was performed in close collaboration with the MACC global reactive gas sub-project and additionally involved the ESA ALANIS Smoke Plumes project.

3.2.6   IFS-TM5

The Western Russian fire episode of 2010 has also been studied with hindcasts of reactive gases produced by the global MACC IFS-TM5 system. Figure 32 compares carbon monoxide (CO) total column simulations to MOPITT observations. The "GFAS" simulation, which is based on GFASv1.0 emissions and has no atmospheric CO assimilation, exhibits a fairly constant bias w.r.t. the

observations. This confirms the accuracy of the GFASv1.0 CO emission magnitude and temporal variability.

Huijnen et al. ACP 2012 also find an improvement of forecasts of ozone, nitrogen dioxide and formaldehyde when GFASv1.0 fire emissions are used instead of climatological ones. Figure 33 illustrates a comparison with independent formaldehyde observations, in which the formaldehyde plume well represented but somewhat overestimated.

When comparing the influence of fire emissions with the one of atmospheric data assimilation, Huijnene et al. ACP 2012 find that the two are complementary and that accurate emissions are particularly important for the forecasting of surface concentrations. Figure 34 illustrates that the fire emission data has a much larger influence on the simulated daily maximum ozone concentration than the assimilation of atmospheric observations. The GFASv1.0 are found to reduce the forecast bias throughout the forecast period and the RMS error for the first three days.
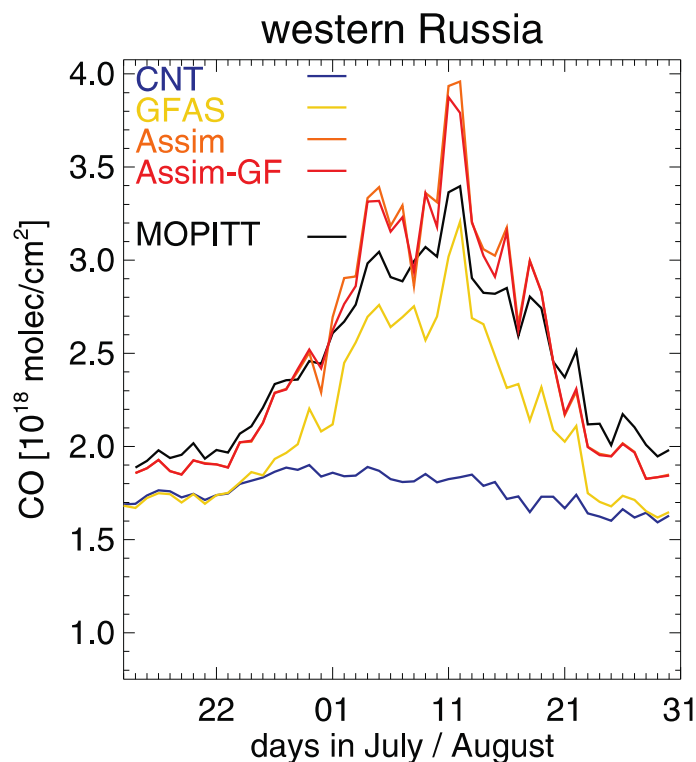

Figure 32: CO column evolution over Western Russia. MOPITT observations and 1-day hindcasts by IFS-TM5 as defined in Figure 31. (Huijnene et al. ACP 2012)
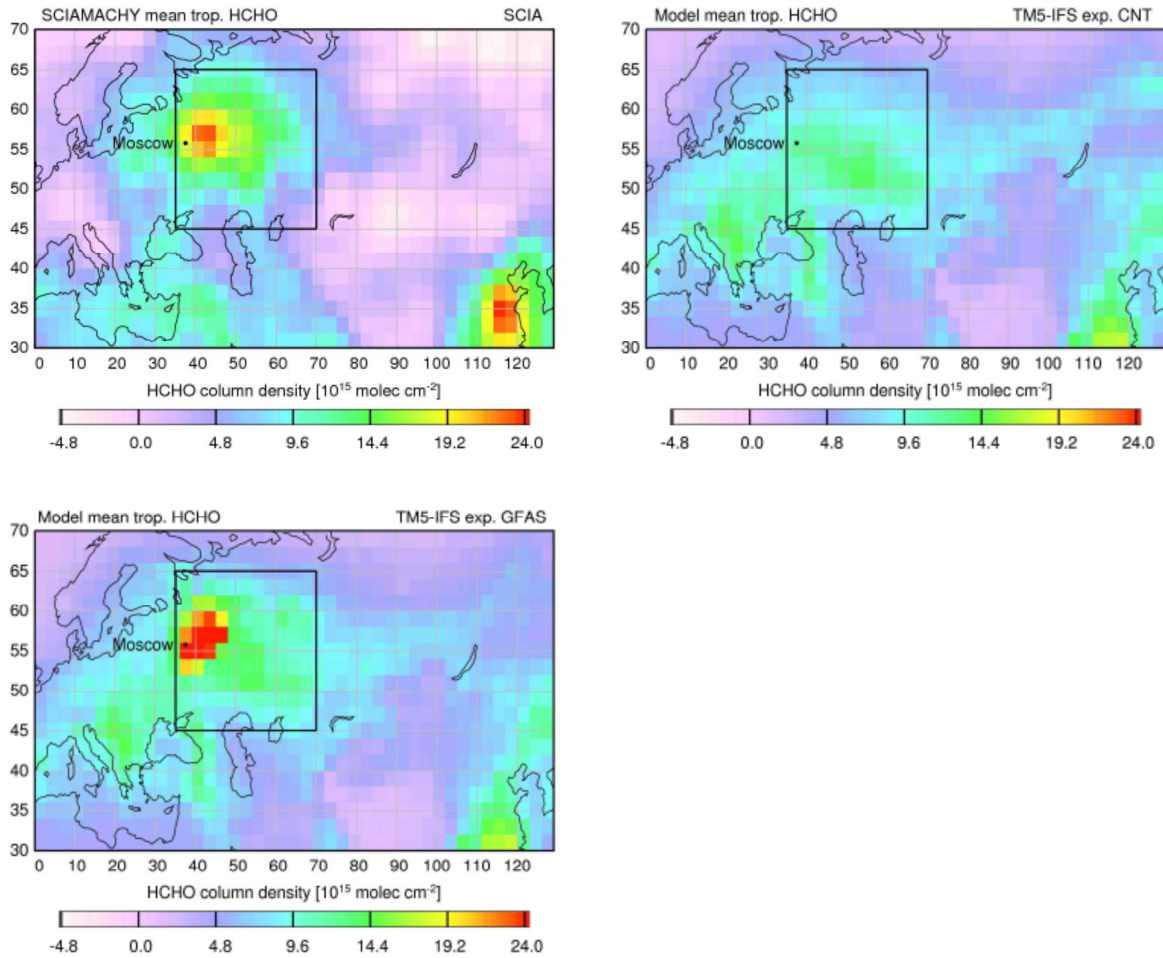
Figure 33: Formaldehyde columns during 20 July and 15 August 2010: SCIAMACHY observations and IFS-TM5 simulations with climatological and GFASv1.0 emissions. (Huijnene et al. ACP 2012)
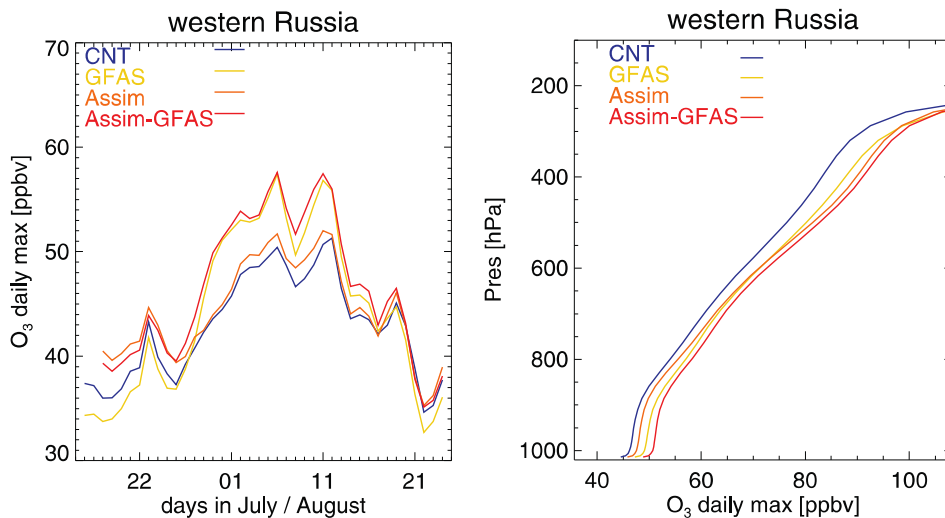

Figure 34: (Left) maximum area-average surface O3 concentrations over Western Russia for the four model settings defined in Figure 31, 1-day hindcast. (Right) corresponding time averaged profile of ozone daily maximum concentrations between 20 July and 15 August. (Huijnene et al. ACP 2012)

3.2.7 MOZART

MOZART sensitivity studies have been carried through employing three different fire emission inventories in standalone simulations for the year 2008, while other emissions were kept unchanged. For these runs the detailed VOC speciation developed for MOZART was used. In a first simulation GFASv1.0 emissions were read into the model on a daily basis. The second simulation used the GFEDv3 monthly fire estimates, while the third simulation was run with a modification of GFASv1.0 using emission factors from Akagi et al. (2011), which is here called GFASv1.0/Akagi. MOZART itself used the same 60 vertical levels as the IFS model with spectral resolution of T63, which corresponds to a horizontal resolution of 1.875°. All emissions are emitted into the lowest level of the model where they are diffused rapidly below the mixing layer height.

Figure 35 and Figure 36 show a comparison of global CO total columns between the model simulations and the corresponding MOPITT retrievals for July and December 2008, respectively. The July maps show a prominent maximum in Southern Africa, which is higher for the simulations than for the satellite retrievals. In December the fire emission maximum is shifted towards Northern Africa, once again with higher values for the model simulations, particularly with GFEDv3 emissions. For most other regions dominated by fire emissions the patterns agree reasonably well in both months.

We also calculated regional mean total columns for selected regions (Figure 37): While all simulations are close to the satellite observations over Europe, larger discrepancies are found for the other regions. Over Eastern Siberia emissions peak in spring and early summer. The higher CO columns for May and June are not found in the simulations but higher values are simulated for January and February 2008. GFEDv3 reveals lower maxima than the other emission inventories for this region. Over tropical Northern Africa the model underestimates the winter maximum while MOPITT finds a distinct minimum in August, which is not seen from the simulations. The agreement for tropical Southern Africa is better, with largest deviations to the satellite retrievals in January and autumn. In general the simulations with GFASv1 and GFEDv1.0/Akagi result in very similar CO columns for all regions. It has to be noted that for a more detailed comparison with satellite total columns the MOPITT averaging kernel information has to be taken into account in order to allow a similar calculation of the column densities. This will be done within the MACC-II project, during which the comparison will also investigate daily fields instead monthly averages.

The differences between the model simulations based on GFASv1.0 and GFEDv3 show that the FRP observations used in GFASv1.0 add regional information to the burnt area observations used in GFEDv3. The similarity to the simulation based on GFASv1.0/Akagi gives an indication that the uncertainty in dry matter combustion rate estimation might be larger than the one associated to species emission factors.
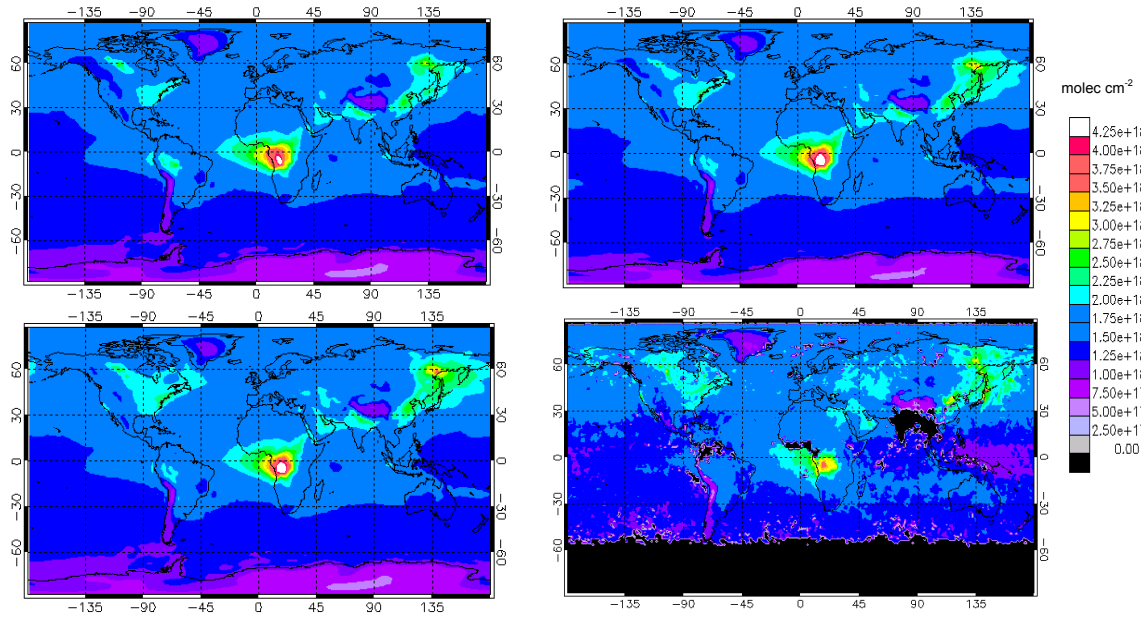
Figure 35: Mean CO total columns for July 2008 from MOZART simulations using GFEDv3 (top left), GFASv1.0, (top right), and GFASv1.0/Akagi (bottom left) fire emission inventories, compared to MOPITT retievals (bottom right)
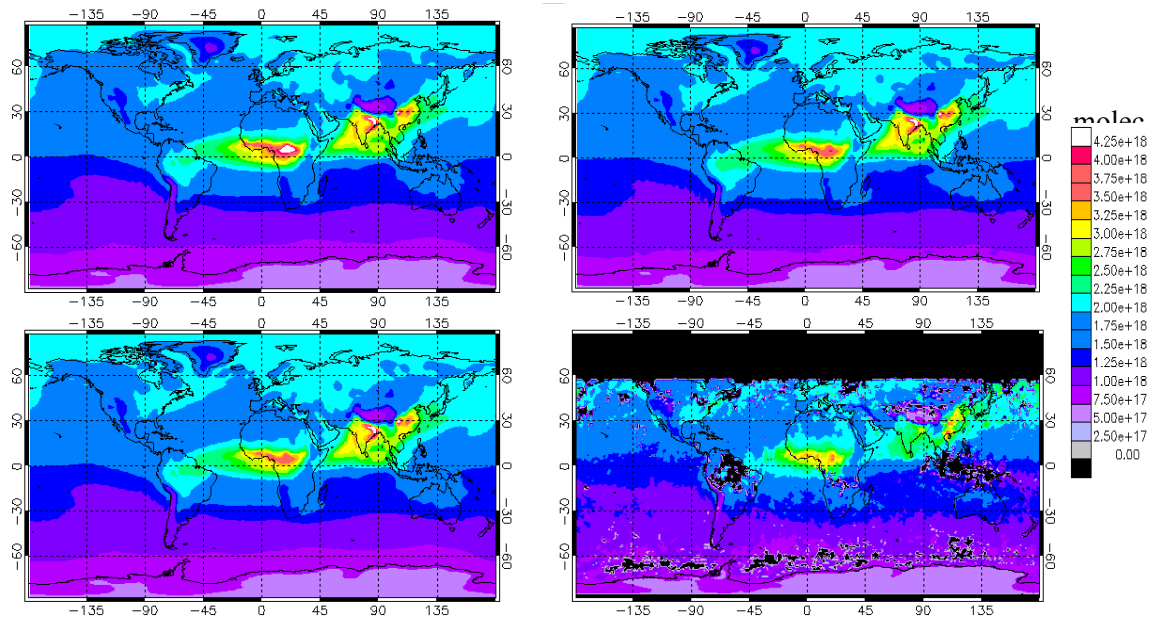

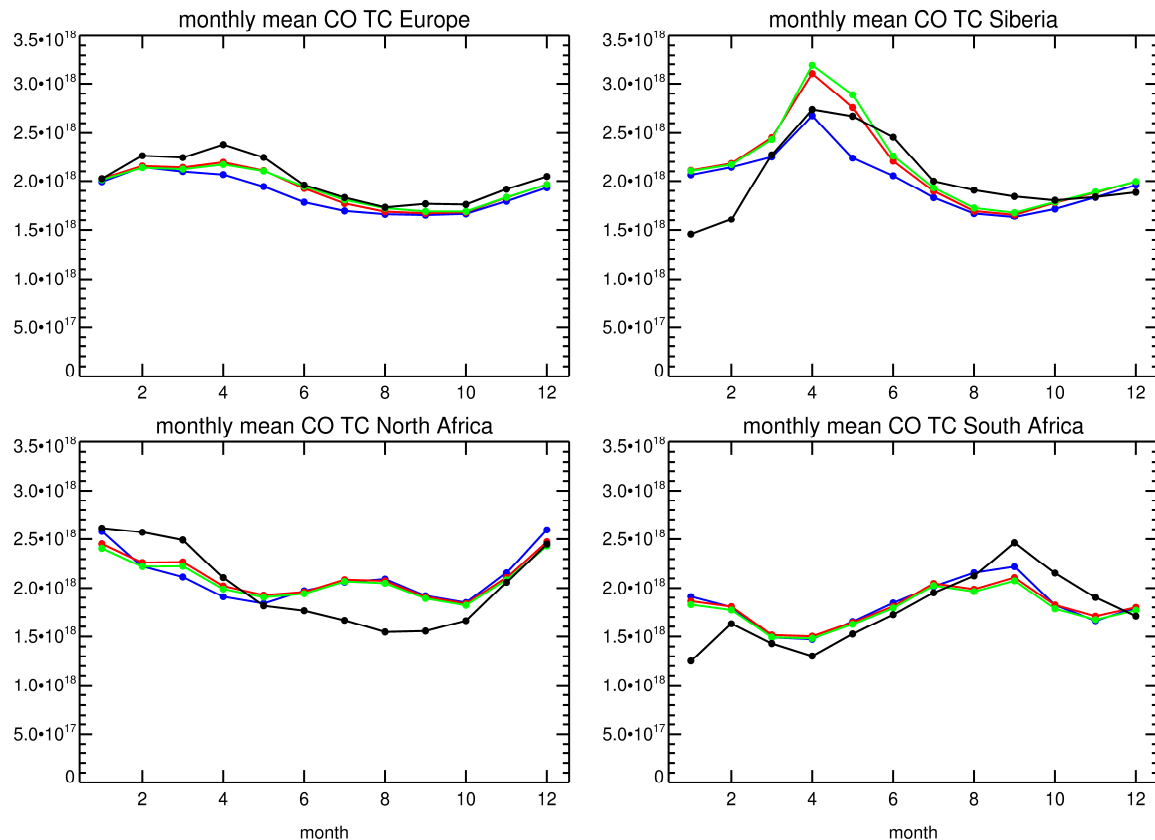*Figure 36: same as Figure 35, but December 2008*

Figure 37: Monthly mean CO total columns [molec cm^{-2}] 2008 for Europe (15°W-35°E, 35°N-70°N), Eastern Siberia (100°E-140°E, 40°N-65°N), Northern Tropical Africa (15°W-45°E, 0°-20°N), and Southern Tropical Africa (15°E-45°E, 20°S-0°) from MOPITT retrievals (black) and MOZART simulation using GFASv1.0 (red), GFEDv3 (blue), and GFASv1.0/Akagi (green) fire emissions.

The MOZART simulations have also been compared for NOx surface mixing ratios (Figure 38 and Figure 39). The patterns related to fire emissions look mostly consistent for the three simulations, but for NOx the GFASv1.0 maxima over Africa resemble more the values from GFEDv3 than those from GFASv1.0/Akagi. A secondary maximum for July 2008 over the Amazonas region is only visible in the GFEDv3 simulation, but not in the runs with the other fire inventories.
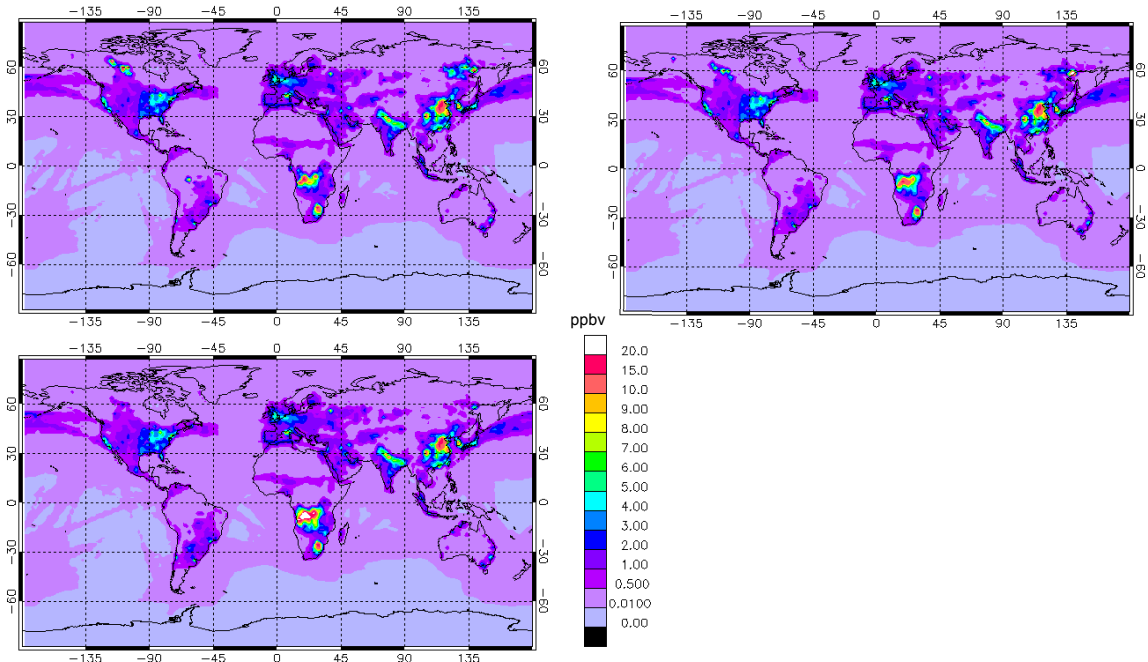
Figure 38: Mean NOx surface mixing ratios for July 2008 from MOZART simulations using GFEDv1 (top left), GFASv1.0, (top right), and GFASv1.0/Akagi (bottom left) fire emission inventories.
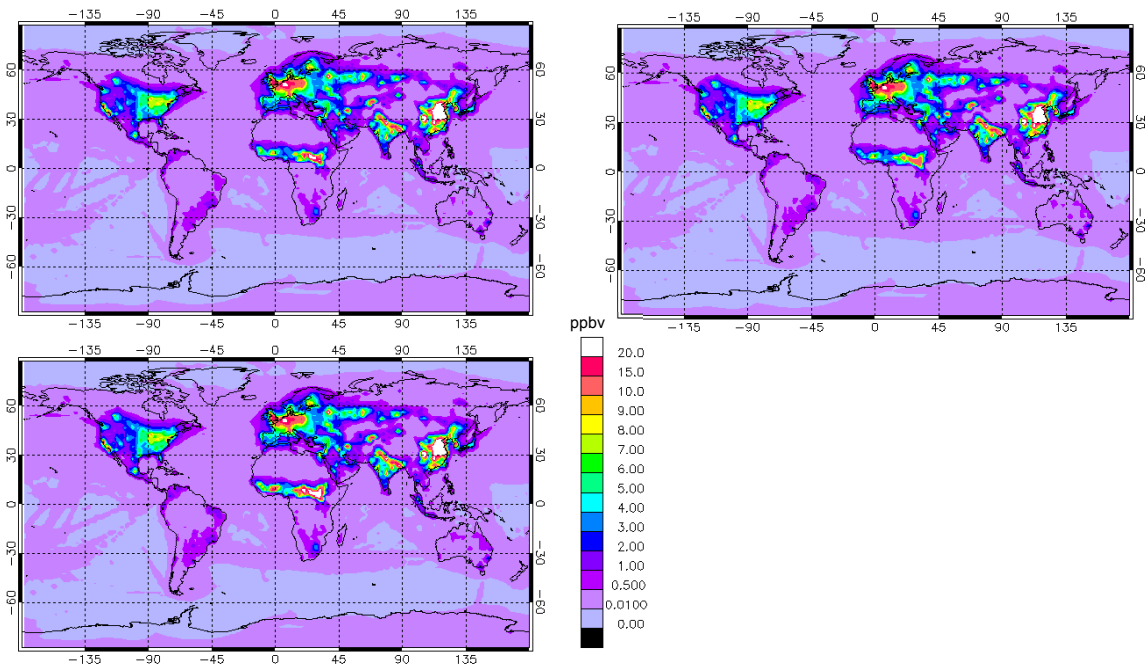

Figure 39: same as Figure 38, but December 2008

3.2.8   Independent regional source inversions of carbon monoxide

An independent study of the pyrogenic carbon monoxide (CO) emissions during the Russian fire episode of 2010 has been performed by Maarten Krol as part of the ESA ALANIS Smoke Plumes project. Atmospheric CO observations by IASI are used to derive "posterior" emission fluxes using an atmospheric model that is driven by "prior" emission estimates. Figure 40 shows that the prior GFASv1.0 CO emission fluxes for the Western Russion fire episode of 2010 agree reasonably well in terms of temporal and spatial distribution with the posterior emission fluxed derived during the inversion. Because of atmospheric mixing it is expected that the posterior fluxes are spatially less localised than the real sources.
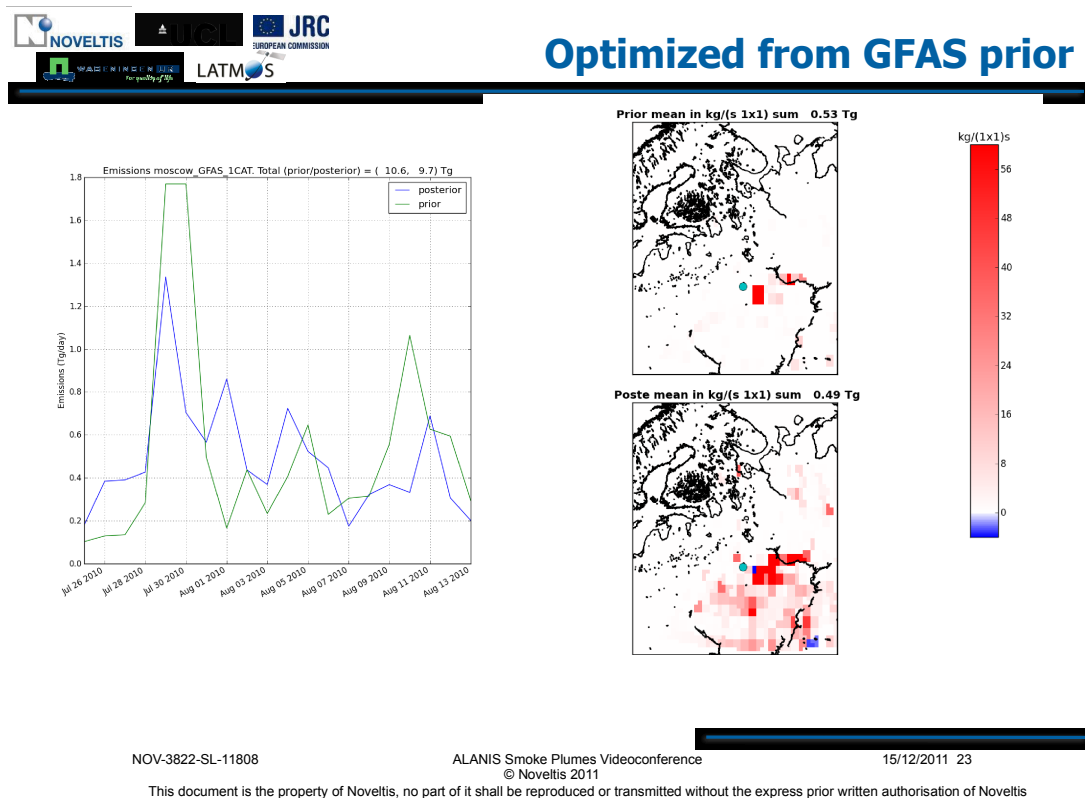

Figure 40: Preliminary CO source inversion of ESA ALANIS Smoke Plumes project using GFASv1.0 as prior. Western Russian fire episode of 2010. (courtesy M. Krol, Wageningen University, now published in Krol et al. ACP 2013)

Figure 41 lists total CO emission budgets for the Western Russian fires of 2010 ("Moscow") and Eastern Siberian ones that occurred simultaneously ("Boreal"). The posterior total emission budgets are fairly independent of the prior emission estimates (MODIS, MERIS, GFAS), which confirm that the inversion yields independent information. For GFAS, the prior and posterior budgets of both the Moscow and Siberian fires agree within 10%, which confirms the high accuracy of the GFASv1.0 products.

Simulation	Emissions (25/7 – 14/8) Tg CO	
	Moscow /	Boreal
Prior MERIS	0.6	1.3
Prior MODIS	1.0	3.1
Posterior MODIS	9.6	14.3
Posterior MERIS	9.3	13.3
MODIS No-SPIH	10.0	14.6
MERIS No-SPIH	9.5	13.5
MERIS (>error)	10.3	13.3
MODIS (>error)	11.2	15.7
MODIS (>>errror)	11.8	10.1 (!)
GFAS Prior	10.6	16.1
GFAS Posterior	9.7	16.6

Figure 41: Preliminary budgets of CO source inversions of Western and Eastern Russia during Summer 2010. (courtesy M. Krol, Wageningen University, ESA ALANIS Smoke Plumes, now published in Krol et al. ACP 2013)

3.3 Other applications

3.3.1 Fire climate monitoring

GFAS has also been used for an assessment of the ECV fire disturbance in the annual NOAA reports *State of the climate in 2009* and *State of the climate in 2010* [Kaiser & Goldammer BAMS 2010, Kaiser & van der Werf BAMS 2011]. Figure 42 shows the biomass burning anomalies of 2009 and 2010 from the reports. They are based on the GFASv0 and GFASv1.0 systems, respectively, and contain only MODIS observations, for which a consistent time series dating back to 2002 exists. In line with the growing confidence in the combustion rates calculated in the latter version of GFAS, the anomaly of 2010 is expressed in terms of carbon combustion rate while the earlier anomaly was expressed in terms of the directly observable FRP.
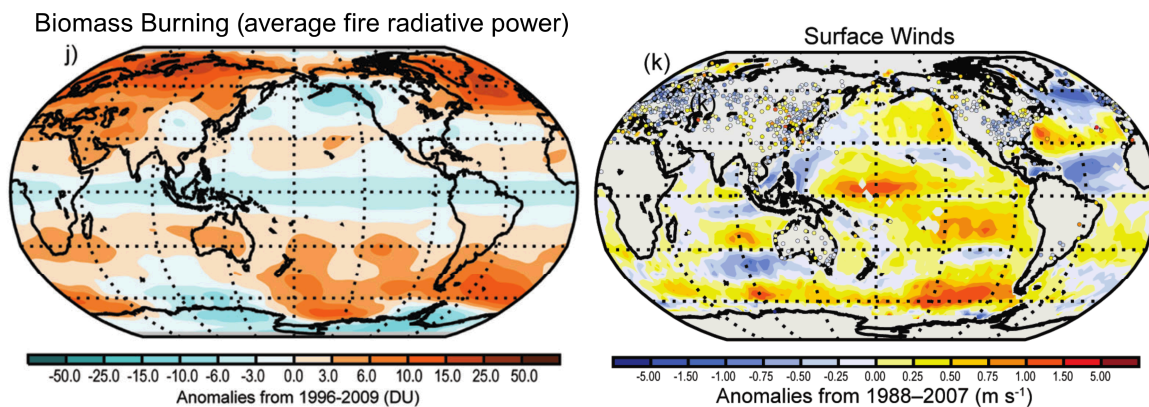

Figure 42: Anomalies of the global fire activity in 2009 (left) and 2010 (right). (Kaiser & Goldammer BAMS 2010, Kaiser & van der Werf BAMS 2011)

3.3.2   Data accessibility

All data products of D-FIRE are publicly available. The sub-project homepage provides a single web entry portal at http://gmes-atmosphere.eu/fire/. It contains, amongst others, a link to a KML product covering the past 10 days. GIF graphics of the daily FRP for the past 375 days are available at http://www.gmes-atmosphere.eu/d/services/gac/nrt/fire_radiative_power/.

CF-compliant NetCDF versions of all GFASv1.0 products dating back to 2003 are available on the interactive and scriptable MACC WCS server platform at http://macc.icg.kfa-juelich.de:50080/access?catalog=http://macc.icg.kfa-juelich.de:58080/MACC_Daily_Wildfire_EmissionsA. All data are archived in MARS, cf. Table 1

Table 1, and provided on request.

3.3.3   Project-external users

Several project-external users have expressed interest in the standard and customised GFED and GFAS data. For example, D-FIRE has compiled emission factors for polycyclic aromatic hydrocarbons (PAHs), dioxins and HCN on-request and calculated the their GFASv1.0 emissions for the MPI Mainz. There was also widespread interest at the EEA-Eionet workshop on GMES services and emission inventories in the GFAS products. Furthermore, there has been interest in the gridded FRP product for other applications than the estimation of emissions from biomass burning, in particular for the monitoring of gas flares and as complementary input for GMES emergency downstream services. An incomplete list of the colleagues who have used GFAS products is:

- Johann Goldammer, Global Fire Monitoring Centre (GFMC), Freiburg University
- Monika Kopacz, Princeton University
- Jessica Ram, NOAA
- Sarah Lu, NOAA
- Anastasia Poupkou, Aristotle University of Thessaloniki
- Gerhard Lammel, MPI Mainz
- Silvia Kloster, MPI Hamburg
- Arlindo da Silva, NASA
- Jeff Reid, NRL Monterey
- Saulo Freitas, INPE-CPTEC
- Qian Li, Chinese Academy of Science, Beijing
- Shobha Kondragunta, NOAA
- Karin Thomas, Forschungszentrum Jülich
- Melita Keywood, Centre for Australian Weather and Climate Research
- Maarten Krol, University of Wageningen
- Meinrat Andreae, MPI Mainz
- Veiko Lehsten, University Lund
- Ellen Baum, Clean Air Task Force

4   Summary

D-FIRE has been providing fire emission data in real time and retrospectively to other MACC sub-projects and project-external users throughout the MACC lifetime. During MACC, D-FIRE has

developed and implemented major upgrades to the retrospective GFED and real time GFAS emission inventory systems. In particular, the new GFEDv3.1 inventory is based on burnt area observations instead of hot spot observations and the new FRP-based GFASv1.0 service has been made consistent with GFEDv3.1 and extensively validated. It also includes an improved FRP satellite product gridding and merging algorithm, new observation quality checks, observation gap filling, a customised land cover map, a novel FRP-to-dry-matter conversion procedure, and updated land-cover-specific emission factors for forty smoke constituents. GFASv1.0 combines the information from the past burnt area observations and past and real time FRP observations.

For the MACC reanalysis, D-FIRE has merged the available products to create a custom emission data set that combines the monthly GFEDv3.0 emission budgets with the daily temporal resolution of a dedicated GFAS version with observation gap filling using a Kalman smoother.

Validation of the aerosol emissions of GFASv1.0 against assimilated MODIS AOD observations in the global MACC service has revealed a discrepancy by a factor of about three between the bottom-up and top-down aerosol emission estimates. This discrepancy is also found in other publishes emission estimates. Therefore, an enhancement of the aerosol emissions by a factor of 3.4 is recommended for the use in global models is recommended. The global MACC aerosol system with enhanced GFASv1.0 emissions reproduces the observed fields and time series of global aerosol and the plume of the Western Russian fires of 2010 in terms of AOD and near-surface PM10.

Several validation studies of the reactive gas emissions during the Western Russian and Siberian fires in 2010 also confirm the carbon monoxide source strength of GFASv1.0. It has been shown that the GFASv1.0 emissions yield information on the near-surface concentrations of carbon monoxide and ozone and the chemical partitioning of aerosols that cannot be obtained by the MACC assimilation of atmospheric composition observations. The accurate fire emission estimation of GFAS is therefore an irreplaceable key element for air quality forecasting during the fire season.

In addition to the proven accuracy of GFAS, there is a large potential for further improvements, in particular through (1) the bias-correction and assimilation of the available geostationary FRP products, (2) the derivation of fire emission forecasts based on past observed fire activity and weather forecasts, (3) injection height estimation, and (4) improved FRP-to-combustion-rate conversion factors and species emission factors. These developments must be guided by integrated assessments and validation in the atmospheric applications of MACC-II.

D-FIRE has been improving the present-day observational input to GFAS by generating real time FRP products from the radiance products of the geostationary GOES East and West satellites and by performing an extensive bias analysis of the FRP product from SEVIRI that is being generated by the EUMETSAT Land SAF. D-FIRE also aims at ensuring the future continuity of the observational input through involvement in the fire product development for the SLSTR instrument aboard the future GMES Sentinel-3 instrument. However, the continued availability of sufficient observational fire emissions for the fire emission monitoring in the GMES Atmospheric Service remains threatened by the inability of ESA to commit to operational FRP production form SLSTR in real time.

The D-FIRE products are documented in the peer-reviewed scientific literature (van der Werf et al. ACP 2010, Kaiser et al. BG 2012, Huijnene et al. ACP 2012) and available for download from public web servers. They are being used by all global MACC services and by project-external users.

5   Publications and References

5.1   D-FIRE presentations

Lammel et al. 'On the contribution of biomass burning to POPs in air in Africa', 6th SETAC World Congress 2012, Berlin, May 2012 [PDF]

Kaiser et al. 'Forest fire NRT emissions', EEA Eionet workshop 'GMES services and emission inventories', Copenhagen, October 2011 [PDF]

Visschedijk et al. 'European Emission Inventory for Four Indicator PAHs for 2005', DioXin 2011, Brussel, August 2011 [PDF]

Huijnen et al. 'Assimilation and hindcast experiments of reactive trace gases during the 2010 Russian fires', EGU GA, Vienna, 2011 [PDF]

Heil et al. 'Validation of MODIS FRP-based Near Realtime Dry Matter Burned Estimates With The Global Fire Emissions Database V3', ESA-iLEAPS-EGU conference, Frascati, 3-5 November 2010 [PDF]

Kaiser et al. 'Global Fire Emission Monitoring with Fire Radiative Power in the MACC Project', Land Surface Analysis SAF 2010 User Workshop, Toulouse, 15-17 November 2010, [PDF]

Kaiser et al. 'From Fire Observations to Smoke Plume Forecasting in the MACC Service', ESA-iLEAPS-EGU conference, Frascati, 3-5 November 2010 [PDF]

Kaiser et al. 'The MACC Fire Products', EGU General Assembly, Vienna, 6 May 2010 [PDF]

Kaiser et al. 'MACC Fire Emission Analysis', MACC General Assembly, Reading, 13 January 2010 [PDF]

van der Werf et al. 'Climate controls on the variability of fires in the tropics and subtropics', EGU General Assembly, Vienna, 3 May 2010

Xu et al. '"Global" Operational Geostationary Fire Radiative Power Data for Supporing NRT Atmospheric Modelling', EGU General Assembly, Vienna, 3 May 2010

Kaiser et al. "Global Real Time Fire Emission Estimation from Fire Radiative Power Observations", GEIA Conference, Oslo, 29 October 2009 [PDF]

Wooster et al. "Estimating Biomass Burnt and Carbon Emissions from Large Wildfires", NERC NCEO Science Meting, 2 - 4 September 2009 [PDF]

Kaiser et al. 'Fire and Plume Monitoring in the MACC Project', EGU General Assembly, Vienna, 3 May 2010 [PDF]

van der Werf et al. 'The improved Global Fire Emissions Database (GFED) version 3: contribution of savanna, forest, deforestation, and peat fires to the global fire emissions budget', EGU General Assembly, Vienna, 3 May 2010

5.2   D-FIRE publications (MACC & GEMS)

Benedetti, A., J. W. Kaiser, and J.-J. Morcrette (2011) [Global Climate] Aerosols [in "State of the Climate in 2010"]. BAMS, 92(6):S65–S67 [PDF]

Freeborn, P.H., Wooster, M.J., Roberts, G. (2011) Addressing the spatiotemporal sampling design of MODIS to provide estimates of the fire radiative energy emitted from Africa, Remote Sensing of Environment, 115, 475-489

Freeborn, P.H., WOOSTER, M.J., Roberts, G., Malamud, B. and Xu, W. (2009) Development of a virtual active fire product for Africa through a synthesis of geostationary and polar orbiting satellite data, Remote Sensing of Environment, 113, 1700-1711

Giglio et al. (2009) Assessing variability and long-term trends in burned area by merging multiple satellite fire products, Biogeosciences 7, volume 7, 1171–1186 [PDF]

Heil et al. (2010) Assessment of the Real-Time Fire Emissions (GFASv0) by MACC, ECMWF Tech. Memo No. 628 [PDF]

Huijnen, V., Flemming, J., Kaiser, J. W., Inness, A., Leitao, J., Heil, A., Eskes, H. J., Schultz, M. G., Benedetti, A., Hadji-Lazaro, J., Dufour, G., and Eremenko, M. (2012). Hindcast experiments of tropospheric composition during the summer 2010 fires over western Russia. Atmos. Chem. Phys., 12:4341–4364. [PDF]

Kaiser, J. W., Heil, A., Andreae, M. O., Benedetti, A., Chubarova, N., Jones, L., Morcrette, J.-J., Razinger, M., Schultz, M. G., Suttie, M., and van der Werf, G. R. (2012). Biomass burning emissions estimated with a global fire assimilation system based on observed fire radiative power. Biogeosciences, 9:527–554. [PDF]

Kaiser, J. W., A. Heil, and G. R. van der Werf (2011) [Global Climate] Biomass Burning [in "State of the Climate in 2010"] BAMS, 92(6):S72–S74 [PDF]

Kaiser, J.W., Benedetti, A., Flemming, J., Morcrette, J.-J., Heil, A., Schultz, M.G., van der Werf, G.R., and Wooster, M.J. (2011a) From Fire Observations to Smoke Plume Forecasting in the MACC Services, Proc. 'Earth Observation for Land-Atmosphere Interaction Science', Frascati, Italy, 3--6 November 2010, European Space Agency, SP-688 [PDF]

Kaiser et al. (2010) Biomass Burning [in "State of the Climate in 2009"] BAMS 91(6) [PDF]

Kaiser et al. (2010a) Understanding the Processes Involved in Biomass Burning, iLEAPS Newsletter No. 9 [PDF]

Kaiser et al. (2010a) Understanding the Processes Involved in Biomass Burning, ECMWF Newsletter No. 122 [PDF]

Kaiser et al. (2009a) Global Real-time Fire Emission Estimates Based on Space-borne Fire Radiative Power Observations, AIP Conf. Proc. Vol. 1100 [PDF]

Kaiser et al. (2009b) The MACC Global Fire Assimilation System: First Emission Products (GFASv0), ECMWF Tech. Memo No. 596 [PDF]

Kaiser et al. (2009c) Smoke in the Air, ECMWF Newsletter No. 119 [PDF]

Kaiser et al. (2009d) SEVIRI Fire Radiative Power and the MACC Atmospheric Services, Proc. 2009 EUMETSAT Met. Sat. Conf. [PDF]

Kaiser et al. (2009e) Understanding the processes involved in biomass burning, IGAC Newsletter No. 42 [PDF]

Kaiser et al. (2009f) Improved Quantitative Fire Description With Mulit-Species Inversions Of Observed Plumes, Scientific Report of European Science Foundation Exploratory Workshop [PDF]

Kaiser, J. W., Schultz, M. G., Gregoire, J. M., Textor, C., Sofiev, M., Bartholome, E., Leroy, M., Engelen, R. J., and Hollingsworth, A. (2006). Observation Requirements for Global Biomass Burning Emission Monitoring. In Proc. 2006 EUMETSAT Met. Sat. Conf. [PDF]

Krol, M., Peters, W., Hooghiemstra, P., George, M., Clerbaux, C., Hurtmans, D., McIn- erney, D., Sedano, F., Bergamaschi, P., El Hajj, M., Kaiser, J. W., Fisher, D., Yershov, V., and Muller, J.-P. (2013). How much CO was emitted by the 2010 fires around Moscow? Atmos. Chem. Phys., 13(9):4737–4747. [URL]

Roberts & Wooster (2008) Fire Detection and Fire Characterization Over Africa Using Meteosat SEVIRI, IEEE TGRS Vol. 46 [PDF]

Schultz et al. (2008) Global wildland fire emissions from 1960 to 2000, GBC Vol. 22 [PDF]

van der Werf et al. (2010) Global fire emissions and the contribution of deforestation, savanna, forest, agricultural, and peat fires (1997–2009), ACPD Vol. 10 [PDF]

van der Werf et al. (2009) CO2 emissions from forest loss, Nature Geoscience 2(11), 737–738 [PDF]

van Leeuwen, T. T. and van der Werf, G. R.: Spatial and temporal variability in the ratio of trace gases emitted from biomass burning, Atmos. Chem. Phys., 11, 3611-3629, doi:10.5194/acp-11-3611-2011, 2011

Wooster, M. J., Xu, W., and Nightingale, T. (2012). Sentinel-3 SLSTR active fire detection and FRP product: Pre-launch algorithm development and performance evaluation using MODIS and ASTER datasets. RSE, 120:236–254.

Xu et al. (2010) New GOES imager algorithms for cloud and active fire detection and fire radiative power assessment across North, South and Central America. RSE Vol. 114 [PDF]

5.3 Other references

Andreae, M. O. and Merlet, P. (2001). Emission of trace gases and aerosols from biomass burning. Global Biogeochemical Cycles, 15(4):955–966.

Hoffman, J. P., Prins E. M., Schmidt C. C., Ackerman S. A., Reid J. S. (2007). Characterizing and understanding the differences between GOES WF_ABBA and MODIS fire products and implications for data assimilation. Symposium on Integrated Observing and Assimilation Systems for Atmosphere, Oceans, and Land Surface, 11th, San Antonio, TX, 14-18 January 2007, *American Meteorological Society*, Boston, MA, 2007, Paper P1.9.

Inness, A., Baier, F., Benedetti, A., Bouarar, I., Chabrillat, S., Clark, H., Clerbaux, C., Coheur, P., Engelen, R. J., Errera, Q., Flemming, J., George, M., Granier, C., Hadji-Lazaro, J., Huijnen, V., Hurtmans, D., Jones, L., Kaiser, J. W., Kapsomenakis, J., Lefever, K., Leitão, J., Razinger, M., Richter, A., Schultz, M. G., Simmons, A. J., Suttie, M., Stein, O., Thépaut, J.-N., Thouret, V., Vrekoussis, M., Zerefos, C., and the MACC team (2013). The MACC reanalysis: an 8 yr data set of atmospheric composition. *Atmos. Chem. Phys.*, 13(8):4073–4109.

Roberts G. and Wooster M.J. (2008). Fire detection and fire characterization over Africa using Meteosat SEVIRI, *IEEE Transaction on Geosciences and Remote Sensing*, 46, 1200-1218.

Schroeder W., Prins E., Giglio L., Csiszar I., Schimdt C., Morisette J., Morton D. (2008b). Validation of GOES and MODIS active fire detection products using ASTER and ETM+ data, *Remote Sensing of Environment* 112, 2711-2726.

Wooster M. J., Roberts G., Perry G. L. W., and Kaufman Y. J., (2005). Retrieval of biomass combustion rates and totals from fire radiative power observations: FRP derivation and calibration relationships between biomass consumption and fire radiative energy release, *Journal of Geophysical Research*, vol. 110, 1415 no. D24, p. D24 311.

W. Xu, M.J. Wooster, G. Roberts, P. Freeborn, New GOES imager algorithms for cloud and active fire detection and fire radiative power assessment across North, South and Central America, *Remote Sensing of Environment,* Volume 114, Issue 9, 15 September 2010, Pages 1876-1895.

Wooster, M.J., Zhukov, B. and Oertel, D. 2003. Fire radiative energy for quantitative study of biomass burning: Derivation from the BIRD experimental satellite and comparison to MODIS fire products. *Remote Sensing of Environment* 86: 83-107.